Università degli Studi di Padova

Physics and Asrtonomy Department

Master Degree in Physics of Data
Fisica

A search for galactic axions with a tunable dielectric cavity in the QUAX–aγ experiment

Supervisor:
Prof. Caterina Braggio

Candidate:
Giosuè Sardo Infirri
2090564

Co-supervisors:
Dott. Giuseppe Ruoso

Academic Year 2023/2024

Abstract

The axion of quantum electrodynamics (QED), which was proposed by Peccei and Quinn to solve the strong charge-parity problem in the standard model (SM) of particle physics, is currently the best motivated cold dark matter (CDM) candidate. The sensitivity required to probe its existence needs the utilisation of resonant detectors, and in particular an high quality factor microwave cavity, which is readout by a very low noise amplifier at the first stage of the electronic amplification chain. The cavity is a cylinder cavity hosting a sapphire shell, designed to obtain high effective volumes at high frequency and quality factors larger than those achievable with empty copper cavities. Furthermore, the need to scan over a wider frequency range requires the cavities to be tunable, via the opening of the copper cylinder with a clamshell mechanism. The receiver that will be employed to readout the cavity is based on a traveling wave parametric amplifier (TWPA), a superconducting amplifier devised to introduce minimum noise, barely exceeding the standard quantum limit (SQL), the level allowed by quantum mechanics.
In this thesis work I show the characterisation of the QUAX dielectric cavity and the working principle of its tuning system at cryogenic temperature. The cavity is then mounted at the lowest stage of the QUAX dilution refrigerator, immersed in a 8T magnetic field, and operated to search for axions with a mass of about 42 μeV. After the characterization of the electronic amplification chain, the experiment is run for a two-week period in two different ignitions: one used as a check for the tuning mechanism and the second as the effective data taken. This procedure allowed a scan of circa 3 MHz per day. After the run I analyzed the data using a procedure similar to the HAYSTAC experiment for both the preventive analysis and the upper limit estimation for the coupling constant $g_{a\gamma\gamma}$.

Contents

Acronyms

ADC Analog to Digital Converter

BCS Bardeen–Cooper–Schrieffer

CDM Cold Dark Matter

CMB Cosmic Microwave Background

CP Charge-Parity

DFSZ Dine-Fischler-Srednicki-Zhitnitsky

DM Dark Matter

EDM Electric Dipole Moment

HEMT High Electron Mobility Transistor

JPA Josephson Parametric Amplifier

KSVZ Kim-Shifman-Vainshtein-Zakharov

LHe Liquid Helium

LNL Laboratori Nazionali di Legnaro

LO Local Oscillator

pdf probability density function

QED Quantum Electrodynamics

SA Spectrum Analyzer

SM Standard Model

SMPD Single Microwave Photon Detector

SNR Signal to Noise Ratio

SQL Standard Quantum Limit

TWPA Traveling Wave Parametric Amplifiers

VNA Vector Network Analyzer

Chapter 1

Introduction

The axion is a hypothetical particle that comes from a solution to a Standard Model (SM) problem, called strong Charge-Parity (CP) problem, and which turns out to have the ideal characteristics for a Cold Dark Matter (CDM) candidate, based on the evidence in favour of dark matter in the context of cosmology[1]. Theoretical models introducing the axion, also establish a particular relation between its mass and coupling constant: to prove the validity of these theories, a sufficiently high sensitivity is required in the experiments, forcing the choice of resonant experimental solutions[2] for an expected axion mass at the μeV level[3]. This Chapter aims to give an overview of the motivations for an axion search, the main experimental challenges presented by the theories and a summary of the main experimental techniques.

1.1 Motivation for axion search

The existence of axions could potentially answer three major open questions in the physical description of our universe: the strong CP problem, the matter-antimatter asymmetry, and the composition of Dark Matter (DM).

The strong CP problem arises from the expected but unobserved CP violation in strong interactions predicted by the SM of particle physics. The CP violation is in fact expected to be governed by the parameter θ_{QCD}: this parameter is also shown to be proportional to the neutron electric dipole moment (EDM)[4]. However, many extremely sensitive measurements were not able to detect the neutron's EDM, suggesting that θ_{QCD} is extremely small, and leading to the idea that strong interactions should not allow CP violation. This possibility is the so-called strong CP problem. The Peccei-Quinn (PQ) theory proposes a solution by introducing a new symmetry involving a dynamic field called axion[5]. This mechanism drives θ_{QCD} to zero, thus solving the strong CP problem and eliminating the expected neutron EDM.

The matter-antimatter asymmetry is another unresolved issue. Although the standard model predicts that matter and antimatter should have been created in equal

amounts, if the initial conditions of the universe did not involve disproportionate matter relative to antimatter, there is no mechanism in the Standard Model to sufficiently explain this asymmetry. The conditions required to create an imbalance, known as the Sakharov conditions[6], include CP violation: from an experimental point of view the CP violation observed in weak interactions is insufficient to explain the observed matter dominance. The PQ mechanism, and in particular the axion field may also contribute to resolving this asymmetry, since a specific scenario called axiogenesis suggests that the rotation of the PQ field in the early universe could generate the excess of matter over antimatter.

Dark matter constitutes about 85% of the universe's matter, as inferred with Cosmic Microwave Background (CMB) angular power spectrum: acquired data perfectly follow the CDM models and no other model is able to reproduce the same results involving visible matter alone.[7] Various candidates for DM have been proposed, with weakly interacting massive particles (WIMPs) being a prime focus in this field: a large number of ultrasensitive experiments looked and is still looking for these particles. Unfortunately, no WIMP has been detected up to now, and the experiment sensitivity is soon going to be limited by the neutrino floor[8]. A second candidate for CDM was then the weakly interacting sub-eV particles (WISPs), such as axions: these newly introduced particles are considered to be the favored candidates for DM because of their weak interactions, long de Broglie wavelengths, and the possibility of forming a Bose-Einstein condensate (BEC), which aligns with some observations of DM behavior.

1.2 A hard-to-be-found particle

Expected axion properties play a crucial role in experimental searches, with a particular attention to their interactions: as with other particles, axion experiments aim to perform an indirect detection. For example the axion mass, which is linked to the scale of symmetry breaking in the PQ mechanism, can be calculated based on its mixing with SM pions. Other axion's interactions involve photons, fermions, and induce EDMs, making them detectable through modifications of Maxwell's equations and anomalous spin precession effects. Experimental searches for axions use these interactions to set exclusion limits in specific sensitivity ranges. The parameter space for axion mass and coupling strength is constrained by both theoretical models and astrophysical observations. For instance, black hole superradiance[9] and supernova cooling[10] provide upper and lower bounds on the axion mass, while observations of star cooling[11][12] further constrain the axion-photon coupling. Two main families of theoretical models, called Kim - Shifman - Vainshtein - Zakharov (KSVZ) and Dine – Fischler – Srednicki – Zhitnitsky (DFSZ)[13], propose different mechanisms for axion interactions with SM particles, impacting the predicted coupling strengths. The models predictions for the theoretical minimal coupling are presented in Figure

1.2 by the two oblique lines. These models give a reference values for the relation between axion mass and coupling constant: experimental efforts, with ongoing and future experiments, aim to narrow down this parameter space further and potentially confirm the existence of axions or otherwise disprove these models.

1.3 Axion experimental search

Axion experimental search begins in 1983 when Pierre Sikivie showed Maxwell's equations modified in the presence of an axion[14]. In the same extent he proposed to reveal axion dark matter bye measure of the photons produced in the axion decay processes. Unluckily we expect a little percentage of axions to decay into photons, due to the weakness of the interaction. This is the main challenge in experimental axion search: we must deal with very small signals. The second problem of this search is the lack of a theoretical prediction regarding the mass of this hypothetical particle: the scanned range spans over several order of magnitudes, as one can see in Figure 1.1. This implies different technologies to be employed, based on the type of axion interaction that they rely on.

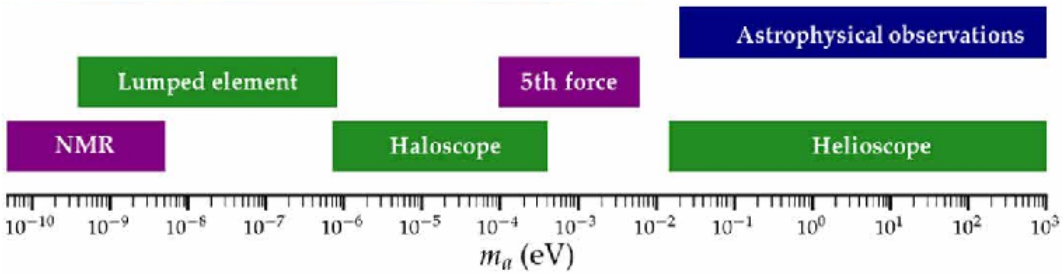

Figure 1.1: Different methods for axion search based on the expected energy in the the most plausible range. They are divided based on the coupling: coupling with the photon (green) and with the nuclear spins (purple) [3]

Experimental efforts mainly rely on the axion interaction with the electromagnetic field, and in particular exploiting the conversion of axions into photons in the presence of a strong magnetic field. We can in fact detect the emitted photons, whose energy corresponds to the axion rest energy: the axion mass is then related to the photon frequency by the Planck relation $h\nu \approx m_a c^2$. This is the main process exploited by axion detection with haloscopes, which are the most sensitive devices we are using for the axion search in mass range from μeV to meV. They are made of a resonant cavity immersed in a strong magnetic field and are suited for the detection of photons that match the cavity frequency: if an axion converts into a photon of this frequency, we expect them to populate the cavity. This should correspond to an increase of the power signal above the system noise. For this reason we expect to have better results when the cavity and the other components introduce the smallest possible amount of noise: we need to operate at ultra-cryogenic temperatures to suppress thermal

noise, and use low-noise amplifiers. Some of such experiments worth mentioning are RBF–UF (Rochester-Brookhaven-Fermilab–University of Florida) [15], ADMX (Axion Dark Matter eXperiment) [16], HAYSTAC (Haloscope at Yale Sensitive to Axion CDM) [17], CAPP (Center for Axion and Precision Physics Research) [18] and QUAX$_{a\gamma}$ (QUaerere AXion) [19], which are presented in Figure 1.2.

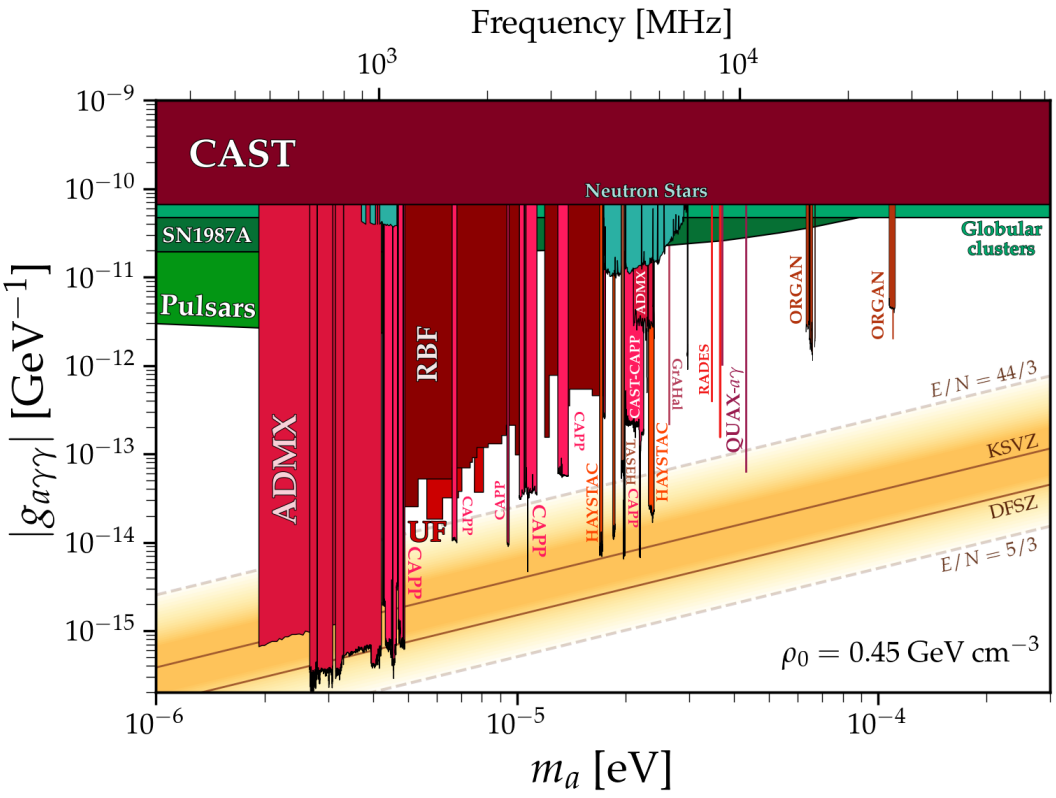

Figure 1.2: Close-up of the axion-photon coupling upper limits for different experiments in the radio frequency region [20] for the converted axion mass

Other experiments use different approaches to detect axions, all relying on the measure of the axion interaction processes, but using other techniques, that can be divided based on the type of interaction:

- Among the experiments that rely on axion-photon coupling, we have to mention Helioscopes, where axions sourced by the Sun could be detected: dipole magnets oriented toward the Sun are used to convert axions into photons, which can be measure via x-ray detectors. Among experiments of this kind, CAST (CERN Axion Solar Telescope) is worth mentioning[21]. A different conceptual approach is used to detect axions coming from all over the universe,

since one can look for axions that have been converted into photons: many experiments rely on astrophysical observations using both space and ground telescopes. This experiment has excluded axions to $g_{a\gamma\gamma} \approx 10\, g_{a\gamma\gamma}^{\mathrm{KSVZ}}$ in the range of mass $[10^{-2} : 10^{2}]$ eV.

- Another coupling possibility is for the axion to couple with the spin of fermionic particles: in particular experiment QUAX_{ae}[22] is using a magnetized sample, in which axion interactions excite the uniform magnetization mode, the Kittel mode. The magnetic mode is coupled to a specific microwave cavity mode to allow for transduction from magnetic excitations in the material to detectable photons in the cavity.
  This experiment has excluded axions to $g_{ae} \approx 10^{3}\, g_{ae}^{\mathrm{KSVZ}}$ in the range of mass $[41.4 : 42]\, \mu$eV corresponding to frequencies $[10.00 : 10.17]$ GHz.

- The last possibility is to measure the axion oscillating field through the measure a time-varying torque on nuclear spins: this effect can be seen either directly or via generation of an oscillating nuclear electric dipole moment (EDM). For both the cases, magnetic resonance techniques can be used to detect such an effect. The pilot experiment in this field is Cosmic Axion Spin Precession Experiment (CASPEr) [23].
  This experiment has excluded axions to $g_{aNN} \approx 10^{2}\, g_{aNN}^{\mathrm{KSVZ}}$ in the range of mass $[10^{-12} : 10^{-6}]$ eV corresponding to frequencies $[10^{3} : 10^{8}]$ Hz.

An important characteristic for these experiments is the sensitivity that they reach, since the most relevant axion models require it to be very high. Another fundamental characteristics for resonant experiments is the scan rate, defined as the velocity at which we can probe the axion parameter space at a fixed sensitivity: due to the huge energy span and the restricted probed range, this quantity determines the parameter space area that the experiment is able to probe.

1.4 Thesis structure

The thesis structure is as follows: in Chapter 2 I will introduce the main theoretical aspects of axions, from the most relevant models and the interaction with photons, as long with a theoretical introduction to resonating cavities and how to couple with its modes. In Chapter 3 I will present the experimental setup, describing working principle of its key components. Chapter 4 will finally describe the data-taking process, as performed in the May-June 2024 data acquisition, and present the performed analysis, after a theoretical introduction on the transition from time to frequency domain.

Chapter 2

A bit of theory

In this Chapter, we aim to introduce the main theoretical aspects of both conception and implementation of the experiment. We start from a brief explanation of the theoretical introduction of the axion as a candidate particle and its physical constraint. Then we will briefly describe the experimental main detector, the resonating cavity, from a theoretical point of view. The implementation of the cavity will be described in Chapter 3.

2.1 Axion models and properties

In quantum chromodynamics (QCD), the theory that describes the strong interactions within the Standard Model of particle physics, the strong CP problem presents an important theoretical challenge. This problem arises from the possibility of a CP-violating term in the QCD Lagrangian density, and in particular in the θ-term:

$$\mathcal{L}_\theta = \frac{g^2}{32\pi^2}\theta F^a_{\mu\nu}\tilde{F}^{\mu\nu a}, \tag{2.1}$$

where $F^a_{\mu\nu}$ is the gluon field strength tensor, $\tilde{F}^{\mu\nu a}$ is the corresponding dual, g is the QCD coupling constant, and finally θ is a parameter that quantifies the amount of violation: in particular, if θ is non-zero, CP violation is introduced in the strong interactions. However, experimental results imply that θ must be extremely small, and in particular of the order of 10^{-10} or less. This contribute comes from two different terms and there is no reason for them to cancel out to such an extent: the absence of an explanation for this balance is known as the "strong CP problem"[24].

2.1.1 Peccei & Quinn solution

A solution to the strong CP problem was proposed by Peccei and Quinn in 1977, who introduced a new global $U(1)$ symmetry, that we will refer as $U(1)_{PQ}$. This symmetry, known as the Peccei-Quinn (PQ) symmetry, is spontaneously broken at

an energy scale f_a, giving rise to a new boson, the axion. The idea behind this model is the introduction of a symmetry whose effect is to suppress the inserted Lagrangian term, and in particular the introduction of a new component of the type:

$$\mathcal{L}_{PQ} = \frac{g^2}{32\pi^2}\frac{a(x)}{f_a}F^a_{\mu\nu}\tilde{F}^{\mu\nu a} \tag{2.2}$$

where a is the axion field. The idea is then for the axion to dynamically oscillate to a value that cancels the θ term in the vacuum averages. In particular one finds out that the Peccei-Quinn potential must have a minimum for the axion field corresponding to $a = f_a\theta$ in order to solve the strong CP problem.

Now the presence of an axion potential generated through non-perturbative QCD effects introduces a mass for the axion particle:

$$m_a = \left.\frac{\partial^2 V_a}{\partial a^2}\right|_{a=f_a\theta} \sim \frac{\Lambda^2_{\text{QCD}}}{f_a} \tag{2.3}$$

where $\Lambda_{\text{QCD}} \sim 200$ MeV is the QCD confinement scale.

2.1.2 KSVZ and DFSZ models

The theoretical prediction of the Peccei and Quinn which expected the axion to have a mass around the electroweak scale have been disproved by the experiments. Thus, the axion currently pursued is light and weakly interacting and the reference models are KSVZ and DFSZ:aA thorough review of axion models is given in [13].

In both these models, axions are predicted to interact very weakly with ordinary matter, making them difficult to detect. Their interactions are primarily through their coupling to photons, gluons, and fermions. The axion-photon coupling is particularly interesting for experimental searches, and in particular for the purposes of this work, with the related term in the SM Lagrangian as:

$$\mathcal{L}_{a\gamma\gamma} = \frac{1}{4}g_{a\gamma\gamma}aF_{\mu\nu}\tilde{F}^{\mu\nu} \tag{2.4}$$

where $F_{\mu\nu}$ is the electromagnetic field strength tensor, while $g_{a\gamma\gamma}$ is the axion-photon coupling constant, which can be expressed as:

$$g_{a\gamma\gamma} = \frac{\alpha g_\gamma}{\pi\sqrt{\chi}}m_a \tag{2.5}$$

where α is the fine structure constant, χ is the zero-temperature QCD topological susceptibility such that $\chi \sim (77.6\,\text{MeV})^4$ and finally g_γ is a dimensionless coupling parameter, whose value is expected to be -0.97 or 0.36 respectively for the KSVZ and the DFSZ model.

As a consequence to the coupling term, and in particular equation 2.4, if an axion is immersed in a strong static magnetic field, then it can interact with a virtual photon provided by the field. This process is visualized in Figure 2.1 and is called inverse Primakoff effect, in which a real photon is generated with an energy corresponding to the axion mass, namely $E_\gamma = m_a c^2$

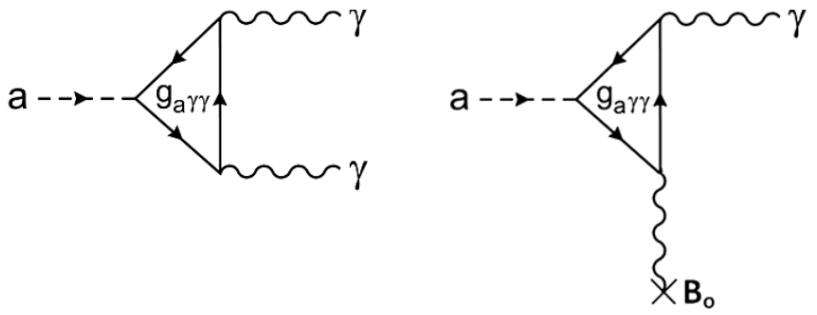

Figure 2.1: Feynman diagram of axion decay into photons: axion conversion in vacuum (left) and inverse Primakoff effect in a static magnetic field $\mathbf{B}_o$ (right) [25]

2.1.3 Cosmological and Astrophysical hints

As briefly explained in the introduction, axions also play a significant role in cosmology and astrophysics, since, if they are sufficiently light and stable, they are the primary candidates for the Cold Dark Matter (CDM). The energy density of axions produced in the early universe via the misalignment mechanism is given by:

$$\rho_a \sim m_a f_a^2 \theta_i^2 \tag{2.6}$$

where θ_i is the initial misalignment angle. This means that, depending on the value of f_a, axions could make up a significant fraction of the cold dark matter in the universe. In addition, axions can impact stellar evolution, since they can be produced in stars and escape without interacting further, leading to an additional channel for energy loss in the stellar evolution. This axion cooling effect has been constrained by observations of stars and supernovae, providing important bounds on axion properties. In particular axion masses lower than $m_a \sim 20\,\mu$eV are excluded.

If we assume the axions to constitute dark matter, we refer to the isothermal sphere model to derive other properties of importance for detector design[26]. In this framework, axion velocities follow a Maxwell-Boltzmann (MB) distribution, and their spectral energy distribution can be derived as:

$$f(E) = \frac{2}{\sqrt{\pi}}\sqrt{E}\left(\frac{3}{m_a\langle v^2\rangle}\right)^{3/2} e^{-\frac{3E}{m_a\langle v^2\rangle}} \tag{2.7}$$

where $\langle v\rangle$ is the average axion velocity. In the earth's reference frame $\langle v\rangle \approx 220$ km/s and the expected quality factor is of the order of 10^6, as shown in Figure 2.2.

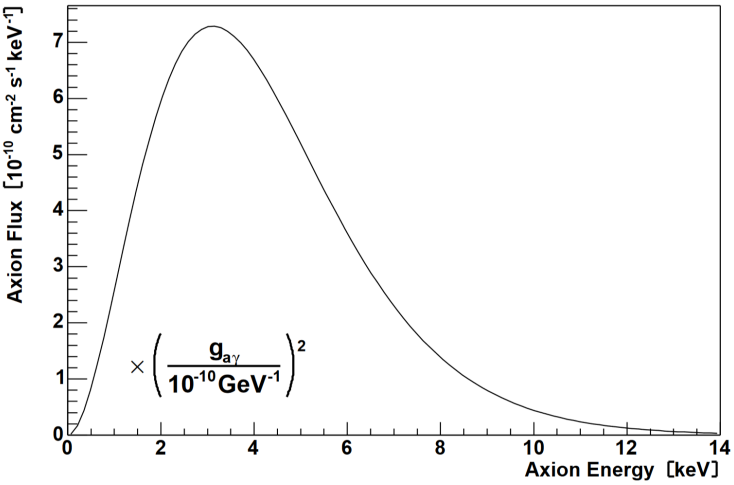

Figure 2.2: Axion flux spectrum on Earth [27]

This quality factor must be known in order to perform the correct analysis, as we will further discuss in Chapter 4.

2.2 Resonant cavities

The central component of the experiment is a microwave cavity, which is used as a fine frequency selector for the axion detection: the requirements for such a cavity are to be tunable, i.e. to have an adjustable frequency, and a very small linewidth, corresponding to an high quality factor. In order to understand the properties of these resonators, one must start from the description of the electromagnetic field in a resonant cavity, and in particular with the solution of Maxwell's equations within a defined volume: these equations are constrained by boundary conditions imposed by metallic walls. The wave equation in the vacuum is then expressed as:

$$\left(\nabla^2 - \frac{1}{c^2}\frac{\partial^2}{\partial t^2}\right)\begin{pmatrix}\mathbf{E}\\ \mathbf{B}\end{pmatrix} = 0 \tag{2.8}$$

Now, if we consider a waveguide with constant cross-section and perfectly conducting walls, which we consider in principle to be true, the boundary conditions are:

$$\mathbf{E}\cdot\hat{n} = 0, \quad \mathbf{B}\times\hat{n} = 0 \tag{2.9}$$

where $\hat{n}$ represents the normal vector to the boundary surface. In cylindrical coordinates (z, ρ, φ), wave solutions travelling along the z-axis can be expressed as:

$$\mathbf{E} = \mathbf{E}(\rho,\varphi)e^{i(kz-2\pi\nu t)}, \quad \mathbf{B} = \mathbf{B}(\rho,\varphi)e^{i(kz-2\pi\nu t)} \tag{2.10}$$

where k is the wave vector, ν is the wave frequency and t is the time. The imposition of these solutions into the wave equation transforms it into the eigenvalue equation:

$$\left(\nabla_\perp^2 + \frac{(2\pi\nu)^2}{c^2} - k^2\right)\begin{pmatrix}\mathbf{E}\\ \mathbf{B}\end{pmatrix} = 0 \tag{2.11}$$

where usually the derivative term is summarized with $\gamma^2 \equiv \frac{(2\pi\nu)^2}{c^2} - k^2$, containing all the physical information on the equation and where $\nabla_\perp^2 = \nabla^2 - \frac{\partial^2}{\partial z^2}$.
The general solutions to this formula form an orthogonal set:

$$\langle \mathbf{E}_2, \mathbf{B}_2 | \mathbf{E}_1, \mathbf{B}_1 \rangle = \frac{1}{2}\left(\int d^3x \epsilon_0 \epsilon(x) \mathbf{E}_2^* \cdot \mathbf{E}_1 + \int d^3x \frac{1}{\mu_0}\mathbf{B}_2^* \cdot \mathbf{B}_1\right) \tag{2.12}$$

where $\epsilon(x)$ is the space-dependent dielectric constant and some solutions are preferred to other: in particular, solutions are categorized as Transverse Magnetic (TM) if $B_z = 0$ or Transverse Electric (TE) if $E_z = 0$.

Each mode has a specific value of resonant frequency and well defined E and B field profiles. To the present work purposes it is central to know all the cavity modes that might interfere (mode mixing) during the cavity frequency tuning with the axion-sensitive mode: in particular those who might couple with the antennas. In fact the interference usually lowers the revealer' sensitivity to zero in some specific frequency ranges, making it impossible for us to acquire data in that specific range.

For a TM solution, the transverse fields can be rewritten as functions of E_z:

$$\mathbf{E}_\perp = \pm\frac{ik}{\gamma^2}\nabla_\perp E_z \tag{2.13}$$

where the positive case applies to the waves travelling in the $+\hat{z}$ direction, while the negative case refers to backward traveling waves.

But we want to describe a cavity and not a waveguide: we must also have to consider a constraint in the $\hat{z}$ direction, which is physically implemented via two perfect conductors in the planes $z = 0$ and $z = d$. The effect of the introduction of these plates is the creation of standing waves between them: by imposing the boundary conditions presented in equations 2.9, one can find that the solutions of the electromagnetic wave equation for the TM modes are:

$$E_z = \psi(\rho, \varphi)\cos\left(\frac{\pi l}{d}z\right), \quad l = 0, 1, 2, \dots \tag{2.14}$$

Now we can move to the cylindrical geometry, since cavities used in haloscopes are usually cylindrical, both for simplicity in the making and for the physical symmetries. In this condition, solutions can be written using Bessel functions $J_m(\rho)$ [28]:

$$E_z^{(mnl)} = E_0 \cos\left(\frac{l\pi z}{d}\right) J_m\left(\frac{u_{mn}\rho}{R}\right)\cos(m\varphi) \tag{2.15}$$

$$\nu_{nml} = \frac{c}{2\pi}\sqrt{\left(\frac{u_{mn}}{R}\right)^2 + \left(\frac{l\pi}{d}\right)^2} \tag{2.16}$$

In literature, modes are then named after these solutions: for instance the magnetic transverse mode presented is named TM_{mnl} mode. Usually cavities that we use in the laboratory are not simple cylinders, due to the presence of dielectric components and the tuning mechanism, which results in a more complex design. In these cases, numerical solutions are computed in order to understand the behaviour of electromagnetic waves in the cavity. These modes can be perceived as perturbations of the theoretically calculated mode, and therefore are usually named in the same way, for instance TM_{mnl} mode.

The choice of the mode is very important, since the power of the axion signal is proportional to the form factor, defined as:

$$C_{mnl} \equiv \frac{|\int d^3x \mathbf{E}_{mnl} \cdot \hat{z}|^2}{V \int d^3x \epsilon(x) |\mathbf{E}_{mnl}|^2} \leq 1 \tag{2.17}$$

where V is the cavity internal volume. If now we assume to have a magnetic field oriented in the $\hat{z}$ direction $\mathbf{B} = B_0 \hat{z}$ and a mode with electric field $\mathbf{E}_\omega$, then the form factor can be rewritten as:

$$C = \frac{\left| \int_V d^3x \, \mathbf{E}_\omega \cdot \mathbf{B} \right|^2}{\int_V d^3x \, |\mathbf{B}|^2 \int_V d^3x \, \varepsilon |\mathbf{E}_\omega|^2} \tag{2.18}$$

From the definition of the form factor, naturally another quantity is derived, called effective volume, and defined as:

$$V_{\mathrm{eff}} = V \cdot C \tag{2.19}$$

This effective volume, as one can see from equation 2.18, can be physically described as the volume where there is an alignment of the electromagnetic radiation and the external magnetic field. This quantity is relevant, since the power deposited on the cavity by the axion wind is proportional to the effective volume: this means that all cavity modes have different axion-sensitivity and that the choice of the mode is relevant for the construction of the cavity and the wanted sensitivity. In particular, in an empty cavity, the form factor is maximal for the TM_{010} mode, commonly used in haloscope experiments.

2.2.1 Important quantities

Cavities are then classified based on their interaction with the electromagnetic radiation, and in particular some quantities have been introduced in order to describe their behaviour. In particular, we want to introduce some quantities that the cavity must satisfy in order to be used in axion search.
In order to determine the useful parameters, it is important to understand that in a resonator, the radiation in a specific frequency range is allowed to go back and forth with a small power loss P_c. The most important parameters are the resonating

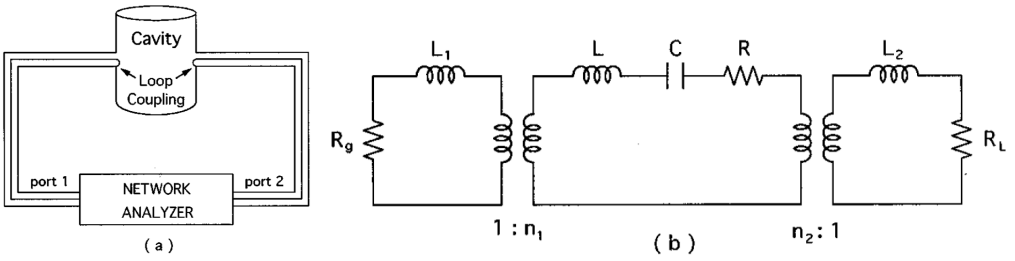

Figure 2.3: (a) Measurement system; (b) Equivalent circuit of a loop coupled cavity

frequency ν_0 and the quality factor Q, which characterizes these losses in a resonator, defined as:

$$Q \equiv \frac{2\pi\nu_0 U}{P_c} \tag{2.20}$$

where U is the energy stored in the resonator and P_c the power lost via Joule heating. These two quantities can be retrieved by means of:

$$U = \frac{1}{2}\epsilon_0 \int_V |\mathbf{E}|^2 \, d^3x = \frac{1}{2\mu_0} \int_V |\mathbf{B}|^2 \, d^3x \tag{2.21}$$

$$P_c = \frac{1}{2\mu_0^2} R_s \int_S |\mathbf{B}|^2 \, d^2x \tag{2.22}$$

These quantities, Q, ν_0 are important for the choice of the resonator, but then one must also keep into consideration the fact that we must coupling to the cavity mode: this means that other losses will enter into play, as we will discuss in Section 2.3

2.3 Coupling to the cavity mode

To readout the cavity signal, transmission lines are coupled to the cavity mode through antennas with coupling coefficient β, defined as the ratio between the power extracted by the antenna P_a and the power internally dissipated by the cavity P_c, namely:

$$\beta \equiv \frac{P_a}{P_c} \tag{2.23}$$

The interaction between the cavity and the antennas can be seen as an electronic circuit, in which the resonator is an RLC-series circuit, while the antennas are some RL-series circuits, coupled with the cavity [29]. The scheme for the description of the cavity-antennas interactions involves two ports and can be analysed using a two-port Spectrum Analyzer, as shown in Figure 2.3. The equivalent circuit elements can be

related to the cavity characteristic parameters:

$$\nu_0 = \frac{1}{2\pi\sqrt{LC}} \qquad \text{resonating frequency} \tag{2.24}$$

$$Q = \frac{1}{R}\sqrt{\frac{L}{C}} \qquad \text{quality factor} \tag{2.25}$$

$$\beta_i = \frac{R_{ai}}{R} \qquad \text{couplings with i = 1, 2} \tag{2.26}$$

We can then evaluate the scattering matrix for this equivalent circuit and see that we can introduce another important quantity for the interaction between the cavity and the antennas, which is the loaded quality factor Q_L defined as:

$$Q_L \equiv \frac{2\pi\nu_0 U}{P_c + P_{a1} + P_{a2}} \tag{2.27}$$

which is related to the unloaded quality factor Q, i.e. the quality factor of the unperturbed cavity, and to the coupling quality factors Q_1 and Q_2 as:

$$\frac{1}{Q_L} = \frac{1 + \beta_1 + \beta_2}{Q} \tag{2.28}$$

$$= \frac{1}{Q} + \frac{1}{Q_1} + \frac{1}{Q_2} \tag{2.29}$$

where $Q_{1,2}$ are the quality factors of the couplings with the antennas:

$$Q_i \equiv \frac{2\pi\nu_0 U}{P_{ei}} = \frac{Q}{\beta_i} \qquad i = 1, 2 \tag{2.30}$$

The power transfer between the two ports is described by a Lorentzian function, with a central resonating frequency ν_0. The loaded quality factor can then be evaluated thanks to the Full Width at Half Maximum (FWHM) $\Delta\nu$, defined as the frequency range in which the transmitted power is higher than half its maximum value:

$$Q_L = \frac{\nu_0}{\Delta\nu} \tag{2.31}$$

Given the link between quality factors and linewidths, we can also link the latter quantity to the cavity linewidth $\Delta\nu_c$, as:

$$\Delta\nu = \Delta\nu_c + \frac{\kappa_1}{2\pi} + \frac{\kappa_2}{2\pi} \tag{2.32}$$

where κ_i are the coupling rates, defined as:

$$\kappa_i \equiv \frac{2\pi\nu_0}{Q_i} \tag{2.33}$$

As it will be detailed in the following, the cavity parameters ν_0, Q and β need to be monitored during data acquisition.

2.4 Deposited power in the cavity

The calculation of deposited power in a resonant cavity is crucial for the comprehension of the energy quantities at play: the deposited power defines the goodness of the apparatus for a set value of the introduced noise.

The starting point for this calculation are the modified Maxwell equations, where the axion-photon interaction is introduced through an additional term, that in particular is mediated by the yet introduced axion-photon coupling $g_{a\gamma\gamma}$. This term leads to the formation of an inhomogeneous wave equation for the electric field $\mathbf{E}$:

$$\nabla^2\mathbf{E} - \frac{\partial^2\mathbf{E}}{\partial t^2} = -g_{a\gamma\gamma}B_0\frac{\partial^2 a(t)}{\partial t^2}\hat{z}. \tag{2.34}$$

where $a(t)$ represents the time-dependent axion field. Note that in this derivation the external magnetic field is B_0 is considered spatially homogeneous, i.e. with $\mathbf{B}(\mathbf{x}) = B_0\hat{z}$ [17], as the axion field varies.
To solve this wave equation in the cavity, we need to introduce the cavity's resonant modes, characterized by orthogonal sets of electric and magnetic fields, denoted by $\mathbf{e}_m$ and $\mathbf{b}_m$ respectively. These modes must obviously satisfy the wave equation:

$$\left(\omega_m^2 + \nabla^2\right)\,\mathbf{e}_m(\mathbf{x}) = 0 \tag{2.35}$$

where ω_m is the frequency of the m-th mode. These $\mathbf{e}_m$ and $\mathbf{b}_m$ form a basis for all the electric and magnetic fields within the cavity: they can then be expanded in terms of these modes, as:

$$\mathbf{E}(\mathbf{x}, t) = \sum_m E_m(t)\mathbf{e}_m(x) \tag{2.36}$$

Substituting the mode expansions into the wave equation and applying the orthogonality condition, we obtain a simplified equation for the mode amplitudes $E_m(t)$:

$$\left(\omega_n^2 + \frac{\partial^2}{\partial t^2}\right)E_n(t) = g_{a\gamma\gamma}B_0\frac{\kappa_n}{\lambda_n}\frac{\partial^2 a(t)}{\partial t^2} \tag{2.37}$$

where κ_n is a geometrical factor related to the cavity mode and $\lambda_n = \frac{2\pi c}{\omega_n}$. The resulting equation is similar to that of an undriven harmonic oscillator with resonant frequency ω_n without a damping term. To take into account losses in the cavity walls, a damping term is added on the left-hand-side: the damping coefficient for a mode with resonant frequency ω_n and quality factor Q_n is its linewidth, thus the introduced term is of the form $(\omega_n/Q_n)\partial_t E_n$. This leads to the frequency-domain expression:

$$\left(\omega_n^2 - \omega^2 - i\frac{\omega\omega_n}{Q_n}\right)E_n(\omega) = g_{a\gamma\gamma}B_0\frac{\kappa_n}{\lambda_n}\omega^2 a(\omega) \tag{2.38}$$

which allows to derive the expression for the amplitude of the electric field:

$$E_n(\omega) = g_{a\gamma\gamma} B_0 \frac{\kappa_n}{\lambda_n} \frac{\omega^2 a(\omega)}{\omega_n^2 - \omega^2 - i\frac{\omega\omega_n}{Q_n}} \tag{2.39}$$

Now, using Parseval's theorem[30] we can derive the energy stored in the cavity as:

$$U_n = \frac{1}{2}\langle E_n(t)^2 \rangle \int_V d^3x \left(|\mathbf{e}_n(x)|^2 + |\mathbf{b}_n(x)|^2 \right) \tag{2.40}$$

$$= \lambda_n \int_{-\infty}^{\infty} \frac{d\omega}{2\pi} |E_n(\omega)|^2 \tag{2.41}$$

$$= \frac{g_{a\gamma\gamma}^2 B_0^2 \kappa_n^2}{\lambda_n} \int_{-\infty}^{\infty} \frac{d\omega}{2\pi} \frac{\omega^4 |a(\omega)|^2}{(\omega_n^2 - \omega^2)^2 + \frac{\omega^2\omega_n^2}{Q_n^2}} \tag{2.42}$$

Finally we can assume that the axion signal is sharply peaked compared to the resonant mode, i.e. $Q_a \gg Q_n \gg 1$, and that the axion frequency ω_a is close to the cavity's resonant frequency ω_n. Under these conditions the integral simplifies, leading to a Lorentzian-like dependence of the energy on the frequency detuning $\delta\omega_a = \omega_n - \omega_a$:

$$U_n = g_{a\gamma\gamma}^2 B_0^2 V C_{nml} \frac{Q_n^2}{1 + \left(\frac{2Q_n \delta\omega_a}{\omega_n}\right)^2} \frac{\rho_a}{m_a^2} \tag{2.43}$$

where $\rho_a = m_a^2 \langle a \rangle^2$ is the DM local density and $C_{mnl} = \kappa_{mnl}/(V\lambda_{mnl})$ is the previously defined form factor. For a mode with frequency ω_c and related loaded quality factor $Q_L = Q_0/(1+\beta)$ we can derive the total signal power:

$$P_{\text{sig}} = \omega_c \frac{U}{Q_L} \frac{\beta}{1+\beta} \tag{2.44}$$

$$= U_0 \frac{\beta}{1+\beta} \frac{Q_L}{1 + \left(\frac{2Q_L \delta\omega_a}{\omega_c}\right)^2} C_{mnl}\, 2\pi\omega_c \tag{2.45}$$

where we U_0 is a constant with dimension of energy:

$$U_0 = g_{a\gamma\gamma}^2 \frac{\hbar^3 c^3 \rho_a}{2\pi\mu_0 m_a^2} B_0^2 V \tag{2.46}$$

Some considerations are worth mentioning: as first the signal power linearly depends on the cavity volume V, and in particular with the effective volume $V_{\text{eff}} = VC_{mnl}$. This means that, for a given frequency, we can increase the cavity's height, at least until mode crowding limits the range that can be probed. Furthermore, since C_{mnl} quantifies the overlap between the cavity mode and the applied magnetic field, lower modes such as TM_{010} are preferred. Most importantly, in the condition of a cavity

with an elevated height w.r.t the radius ($d \gg R$) and considering Q to be independent on the frequency, as the resonant frequency $\nu_c = 2\pi\omega_n$ is inversely proportional to the cavity radius, namely $\nu_c = \frac{c \cdot u}{2\pi R}$, the signal power scales as $P_{\text{sig}} \propto \nu_c^{-1}$. In facts cavities with a smaller radius yield higher frequencies but reduce the overall volume: therefore for a fixed frequency, other optimizations must take place, as the insertion of dielectric materials, in order to improve the signal power and the scan rate.

2.5 Noise Temperature and Scan rate

In axion haloscope experiments, given the wide area of the parameter space to be probed and the restricted frequency range that one can probe with a resonator, it is important to take into account the time needed for the experiment to be run. For this reason a critical parameter has been introduced, called *scan rate* $\frac{df}{dt}$: it refers to the rate at which the experiment can probe different axion masses within a given time period, for a specific sensitivity or signal-to-noise ratio (SNR). Given the uncertainty in the axion mass, it is essential to design experiments that can effectively scan across a wide frequency range while maintaining an high sensitivity. The scan rate depends on several factors, regarding the apparatus design, the amount of time needed and axion properties.

A key parameter is the system noise temperature T_{sys}, also called Johnson–Nyquist noise. It is a measure of the noise power relative to the thermal noise at a given temperature, mathematically defined as:

$$T_{\text{sys}} = \frac{P_{\text{noise}}(\Delta\nu)}{k_B \Delta\nu} \tag{2.47}$$

where k_B is the Boltzmann constant, $\Delta\nu$ is the frequency range over which the measure is made and the system noise power P_{noise} includes contributions from both the physical temperature of the cavity and electronic noise[31]. Since we are comparing the system power to the noise generated by a source at a specific temperature, we are assuming it to follow a Gaussian distribution, whose fluctuations are expected to follow the Dicke's equation:

$$\sigma_D = k_B T_{\text{sys}} \frac{\Delta\nu}{\Delta t} \tag{2.48}$$

once sampled for a time interval Δt. The signal-to-noise ratio (SNR), and in particular, from the Dicke radiometer equation, we know that:

$$\text{SNR} = \frac{P_{\text{sig}}}{\sigma_D} = \frac{P_{\text{sig}}}{k_B T_{\text{sys}}} \sqrt{\frac{\Delta t}{\Delta\nu}} \tag{2.49}$$

where P_{sig} is the signal power expected by an axion in the $\Delta\nu$ frequency range, as retrieved in Section 2.4. The expression can be inverted to highlight the amount of

time required to reach a fixed SNR value for any bandwidth $\Delta\nu$:

$$\Delta t = \left(\frac{\mathrm{SNR}\, k_B T_{\mathrm{sys}}}{P_{\mathrm{sig}}} \right)^2 \Delta\nu \tag{2.50}$$

From this formula we can see that the the optimal value for the frequency resolution is $\Delta\nu = \Delta\nu_a$ the axion linewidth: this can easily be explained since, if we take a smaller resolution, then the axion power is divided in many frequency regions and we are not improving the ratio between power and frequency, while if we take a bigger resolution, then we are introducing only noise power. From this formula we can then retrieve the scan rate as:

$$\frac{\Delta\nu}{\Delta t} = \left(\frac{P_{\mathrm{sig}}}{\mathrm{SNR}\, k_B T_{\mathrm{sys}}} \right)^2 \tag{2.51}$$

This formula tells us the importance of both reducing the system noise temperature and increasing the signal power, in order to optimize scan rate for a fixed SNR: this will lead to the optimized scan over the parameter space. In particular the experiment has been designed in order to increase the scan rate as much as possible. In particular the cavity has been realized in order to maximise the effective volume and to have a quality factor as high as possible. Furthermore, since the signal power scales quadratically with B_0, superconducting magnets are typically employed in haloscope search with field amplitudes in the range $8 - 12$ T. These are commercially available magnets, but it is worth mentioning that there are experiments using custom magnets that could go up to 18 T[32]. This increment in the magnet power therefore improves the scan rate. Moreover, tuning the cavity's coupling parameter β allows for optimization of the signal extraction, with critical coupling $\beta = 1$ providing an optimal balance between power extraction and energy storage. Unluckily, this choice of β is quite poor for signal power and scan rate: the optimal value in this sense is reached using $\beta = 2$, forcing experiments to work in this condition.

Chapter 3

Experimental setup

In this Chapter, we will describe in detail the main experimental components and their working principle. An haloscope is in fact mainly comprised of three principal components: a resonating cavity, a refrigerating system able to keep the cavity at cryogenic temperatures and finally an electronic chain for signal amplification and readout.

3.1 Haloscope in a nutshell

The axion haloscope has proven to be the most successful experimental design in the search for Cold Dark Matter (CDM) axions, for its good performances on the signal-to-noise ratio (SNR). Thanks to its resonant working principle, the haloscope is a very sensitive detector, making it perfect for high-sensitivity measurements: it allows to resonantly enhance the signal and to isolate it from sources of noise at a specific frequency.
We owe the introduction of the axion haloscope to Pierre Sikivie, who, in 1983, proposed that the interaction of axions with the electromagnetic field mediated by pions could be utilized for axion detection in the presence of strong magnetic fields [14]. The power spectrum of the resulting signal is extremely sharp and, as briefly described in Section 2.1, could be approximated by a Maxwell-Boltzmann distribution. The basic idea is to enhance the power transfer by using a microwave resonant cavity tuned to the frequency corresponding to the axion mass, given by:

$$\nu_a = \frac{E_a}{h} = \frac{m_a c^2}{h} \approx 0.1 - 100 \text{ GHz} \tag{3.1}$$

where the upper/lower bounds are constraints of the physical implementation, i.e. the dimension of the cavity. The effect of the resonating cavity is the integration of the signals over time, as described in Section 2.4, which results in an amplification of the collected signal by a factor equal to the loaded quality factor of the resonant mode, as long as it is not higher than the equivalent quality factor of the axion power

spectrum. This deposited power is then detected as excess power during the analysis of the noise spectrum of the apparatus, as we will describe in Chapter 4.

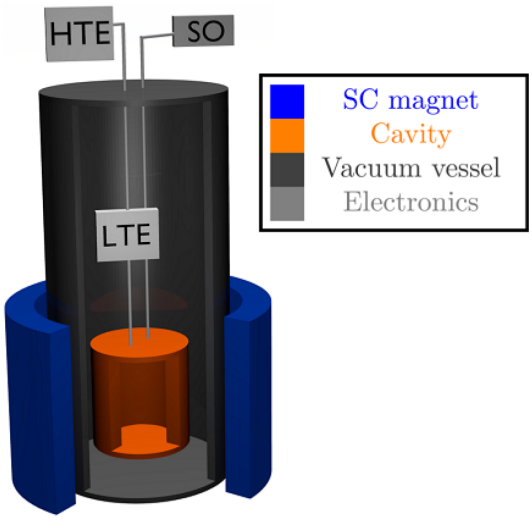

Figure 3.1: Schematic apparatus of an axion haloscope, where HTE stands for the Room temperature electronic chain, LTE stand for the Cryogenic electronic chain and SO is the Source Oscillator. Credits to [33]

The fundamental elements of an axion haloscope, as depicted in Figure 3.1, are the following:

- **Microwave tunable cavity**: the principal component of the system is a high quality factor superconducting tunable cavity, which is a cylindrical hole in a superconducting material, as described in Section 2.2. The signal selected by the cavity frequency is collected through a tunable antenna, which can achieve critical or more-than-critical coupling conditions, where we recall that they are respectively met for $\beta \sim 1$ and $\beta \gtrsim 1$. The most important characteristic for haloscope cavities is then a mechanisms to tune the measurement mode's frequency: this allows to scan among a frequency range larger than a single cavity linewidth, and is therefore the key principle of these haloscopes;

- **Cryogenic electronic chain**: it comprises low noise microwave amplifiers and RF components such as circulators, isolators, and filters. In order to have optimal SNR, it is important to have a first amplification at cryogenic level, since the first amplifier is the one introducing the biggest amount of noise. In fact the total noise temperature of the amplification chain for the gains G_i and the equivalent noise temperatures $T_{n,i}$ for the i-th amplification constituent, can be evaluated as:

$$T_{\text{amp}} = T_{n,1} + \frac{T_{n,2}}{G_1} + \frac{T_{n,3}}{G_1 G_2} + \cdots \tag{3.2}$$

where it is straightforward that the first amplification stage is the most relevant, since it is not attenuated by the previous amplifiers.

- **Room temperature electronic chain**: this section of the electronics receiver includes amplifiers, low-pass filters, and an Analog-To-Digital Converter (ADC). A component typically used to down-convert the frequency of signals in microwave receivers is the mixer: this allows for data size reduction without losing any physically relevant informations. Data are finally converted to digital in the ADC and stored: frequency spectra can be reconstructed using the Fourier Transform of the saved signals in the phase and quadrature components;

- **Strong magnet**: given the squared dependence of the axion deposited signal with the strength of the magnetic field, as described in Section 2.4, a very strong magnet is needed. Given the mode profile in a cylindrical cavity, a solenoidal shaped magnet is used: it completely surrounds the cavity and provides a uniform strong magnetic field in all the cavity volume. As superconducting electronics, and in particular the TWPA, are not compatible with the intense magnetic field required in this search, they are actively screened by an additional coil whose aim is to suppresses the main B_0 field. Additional protection to these component is ensured by enclosing them within boxes of cryoperm, which acts as a further passive screen. Usually, for the vicinity to the cavity, a superconducting magnet is used;

- **Cryogenic vessel**: The cavity and cryogenic receiver's components are operated inside a wet dilution refrigerator with 50 mK base temperature. Only the cavity, the circulator and the first stage of amplification are attached to this lowest temperature stage as shown in Figure 3.6a, in order to ensure the amplifier to work properly and to suppress the thermal photons coming from the cavity. The second amplifier is connected to the plate at liquid helium temperature $T_{\mathrm{He}} = 4.2$ K; the superconducting magnet is fully immersed in the same liquid helium bath to ensure operation of the magnet below the superconductor coil critical temperature.[(1)]

The previously described components must be carefully chosen in order to have the highest possible axion sensitivity, which in fact depends on various factors, including the quality factor of the resonating cavity, the strength of the magnetic field and the thermal noise of the system. In the high-frequency regime considered in this work, which is at around 10 GHz, a careful optimization of these parameters is required in order to achieve a sufficient sensitivity: each component is then tested in the calibration procedure, in order to satisfy the required characteristics.

[(1)]The magnet is typically made in NbTi, whose critical temperature is in the range $[6 : 9]$ K depending on the magnetic field [34]

3.2 Tunable cavity

In Section 2.2 we described the working principle of a resonating cavity and its characteristic parameters: in this Section we will give a description of the cavity we used and its features. We used a cavity containing a cylindrical dielectric, which allows to have an effective volume 10 times higher with respect to an empty cavity, for the search of axions at higher frequencies, around 10 GHz.

As pointed out in Section 2.4, cavities used for axion detection are required to maximize the overlap between the electric field and the external magnetic field, and in particular the effective volume. This condition is satisfied by the TM_{010} mode of the cylindrical cavity: in fact it allows to have a stronger field along the entire radial component compared to higher-order modes, as shown in Figure 3.2a. For this reason it is the mode used in conventional haloscopes.
To date, haloscope experiments have probed the range [600 MHz : 1 GHz] at DFSZ sensititivy with cavities of several tens of liters and magnets with a bore of tens of centimetres[35]; similar experiments are approaching the KSVZ sensitivity in the range [1 : 5] GHz [36][37]. In the interval down to 100 MHz experiments still involve the use of large cavities and magnets. In fact, for lower frequencies, bigger cavities are required, and in particular magnets able to create a strong and uniform magnetic field with a bore bigger than the cavity diameter: this represents the main challenge in low-mass axion search. At frequencies above 5 GHz, the main limitation is set by the unfavourable scaling of the scan rate with respect to the probed frequency: $\frac{df}{dt} \propto f^{-4}$. Other solutions are required to compensate this scaling and therefore allowing to work in this frequency range.

To probe for higher frequency axions with relevant sensitivity, one might consider higher order TM modes in the cylindrical resonator. However, their C factor is too small as shown in Table 3.1:

Cavity mode	C-factor
TM_{010}	0.61
TM_{020}	0.12
TM_{030}	0.17

Table 3.1: Value of the C-factor for the first three TM modes in an empty cavity

This result is explained by the presence of negative lobes in the electric field behaviour, as shown in Figure 3.2a: the presence of electric fields opposite to the external magnetic field, significantly reduces the effective volume, and consequently the sensitivity.
The effect of these negative lobes can be diminished by inserting properly shaped dielectric shells: the idea is to reshape the electric field profile placing the dielectric material in correspondence of the lobes, thanks to the high value of its dielectric

constant $\epsilon_r = \epsilon_0 \kappa_r$. The optimal dielectric shape for the suppression of negative components in the cavity fields is an hollow cylinder, also called shell, as shown in Figure 3.2b: thanks to this particular object, larger effective volumes at given frequency can be accomplished compared to the conventional ones. Furthermore larger quality factor can also be obtained in certain configurations, as the resulting field profile is such that ohmic losses are smaller at the copper boundaries.

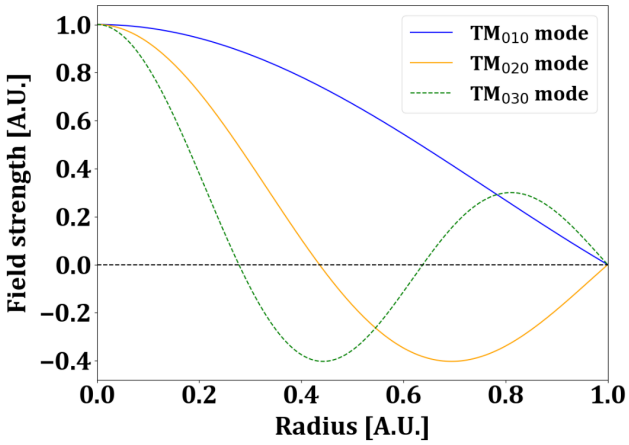

(a) Modes of the cylindrical cavity

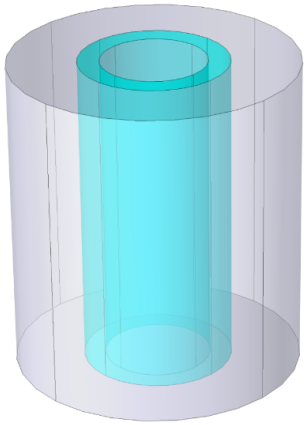

(b) Dielectric position in cavity

Figure 3.2

The effect of the insertion of the dielectric material on the TM_{030} mode is visible in Figure 3.3 for the insertion of one or two concentric dielectric shells. One can clearly see that this insertion strongly affects the electric fields radially and consequently the effective volume, allowing for the axion search at higher frequency w.r.t. the use of TM_{010} mode. In our experiment, the chosen material for the dielectric component is the sapphire, with $\kappa_{\text{sapphire}} \sim 11.5$.

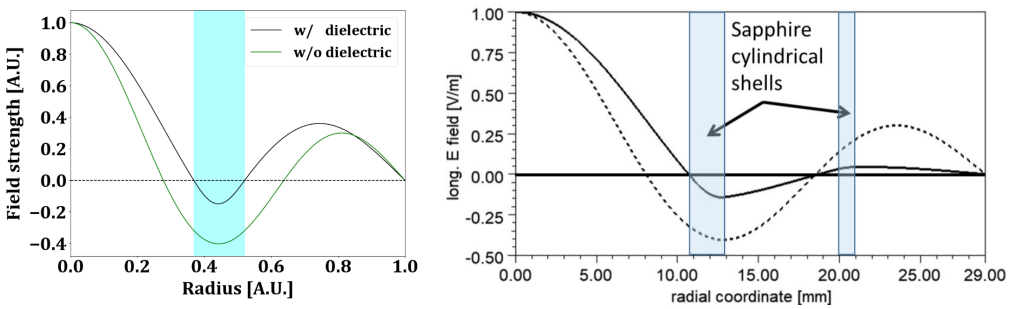

Figure 3.3: Mode TM_{030} profiles with and without the insertion of one (left) or two (right) dielectric shells [38]

3.2.1 Cavity Tuability

The goodness of an haloscope also relies on its ability to scan the maximum possible frequency range, since the axion mass is unknown. Many techniques have been introduced and all of them require to mechanically interact with the cavity in order to perturb the measurement mode and therefore alter its frequency. The main technique used up to now required the insertion of some dielectric rods from one of the cavity endings. These rods changed the field in the terminal part of the cavity, altering the mode and in particular its frequency.

Figure 3.4: Cavity used, showing the aperture into two halves and the return springs

The resonator used in this work can be tuned by opening the external copper cylinder with a clamshell mechanism: the external copper body is in fact divided into two halves cut along the cylinder axis, which are radially separated while joined at a fixed edge[39]. The mechanism controlling the opening angle relies on a 2.2 meters long stainless steel wire that connects a high-resolution stepper motor (Mod. PI M-230.2SS) operated at room temperature, to a conical wedge used to separate the two copper shells. The force applied by the wedge is balanced by four springs mounted next to it, as shown in Figure 3.4, and near the top and bottom cavity endcaps. As might be expected, in this type of mechanism hysteresis effects have to be taken into account when the cavity is opened starting from the closed position, corresponding to a null opening angle. As shown in Figure 3.5, the mechanism performs well, i.e. there is linearity between stepper motor position and opening angle, and therefore the frequency, but there are "jumps" that might be ascribed to sudden relaxations of the spring system. For these frequency intervals, rescan needs to be considered to ensure a uniform data acquisition in the planned axion mass interval. In future realizations of this apparatus, we are considering to replace the wire with a tiny rod to open the cavity, which is a more conventional rigid system: in particular the realization of a reliable mechanical apparatus is required to ensure a correct scan.

The clamshell principle represents a more challenging fabrication in order not to consistently change the quality factor, but allows to span across a range that is a hundred times wider w.r.t. the rods implementation. In the present apparatus a tuning range of approximately 60 MHz was demonstrated, which allowed to probe for axion masses in the range $41.3 \div 42.6$ μeV. In principle, a much broader range of

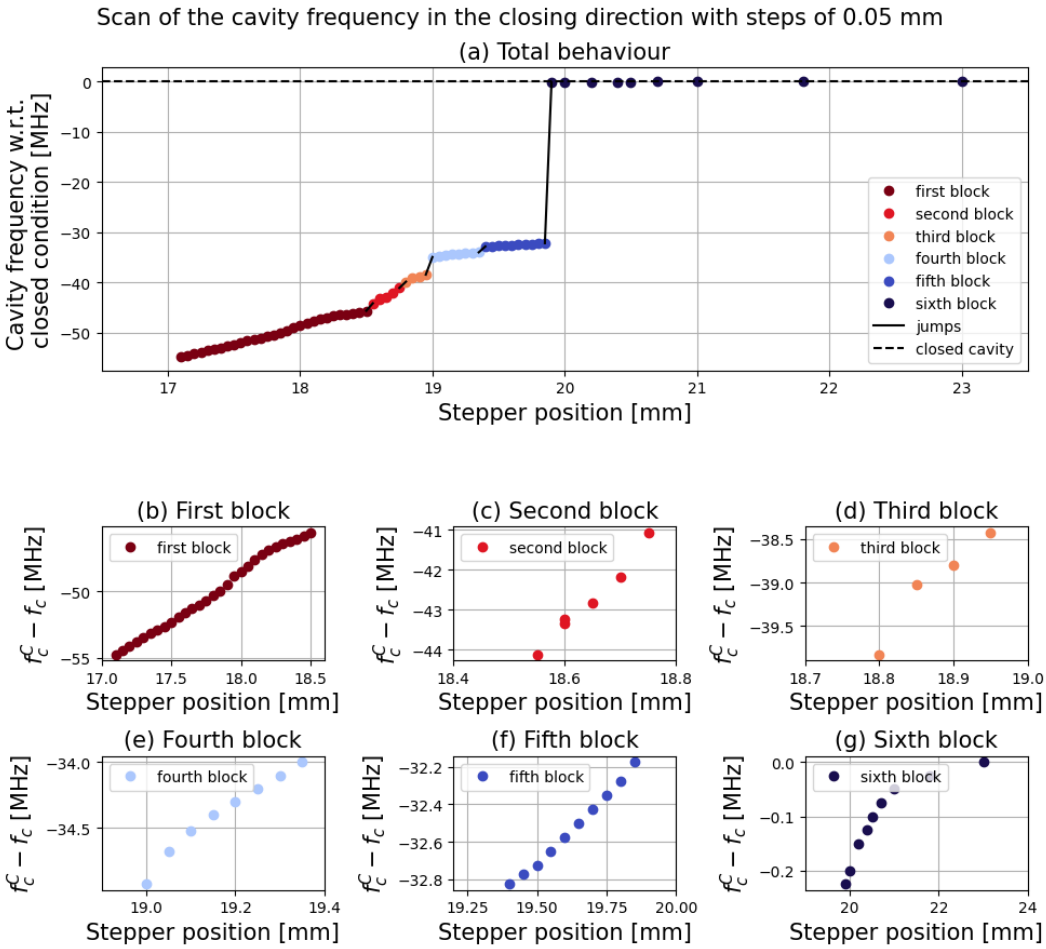

Figure 3.5: Scan of the cavity frequency using the stepper in the closing direction, i.e. from the opened condition (red) to the closed one (blue): (a) shift of the cavity frequency with the stepper set to 0.05 mm sized steps, with; (b - g) the resulting blocks separated by the jumps, which show an almost linear behaviour

approximatively 200 MHz might be accomplished with this mechanism, as shown by the results of finite-difference method simulations. The probed frequency range can be confronted with the $\sim$ 6 MHz range obtained using dielectric rods with a previous version of this cavity[40].

This difference strongly supports this newly introduced mechanism and shows that the cavity tuning represents one of the most important challenges for haloscopes optimization: other mechanisms have been probed [39] but all of them suffer the same reliability problem, given the presence of hysteresis at cryogenic temperatures.

3.3 Electronic chain

The electronic chain is mainly divided in two parts: the cryogenic part (Figure 3.6a), which is responsible for the amplification of the detected signals at low temperatures, and the room temperature part (Figure 3.6b), which is on the other hand responsible for the signal digitalization. The two parts are connected via some switches (Figure 3.8), that allow us to change the configuration of input/output between the three lines of the two parts without any human intervention: this set of switches, as we will later see, is of fundamental importance in the calibration of the system. In particular, the electronic is comprised of three lines (L1, L3, L4) for the connection to the cavity: three lines are needed for the Noise Temperature evaluation, as will explained in Section 3.5, and for the antenna's coupling evaluation.

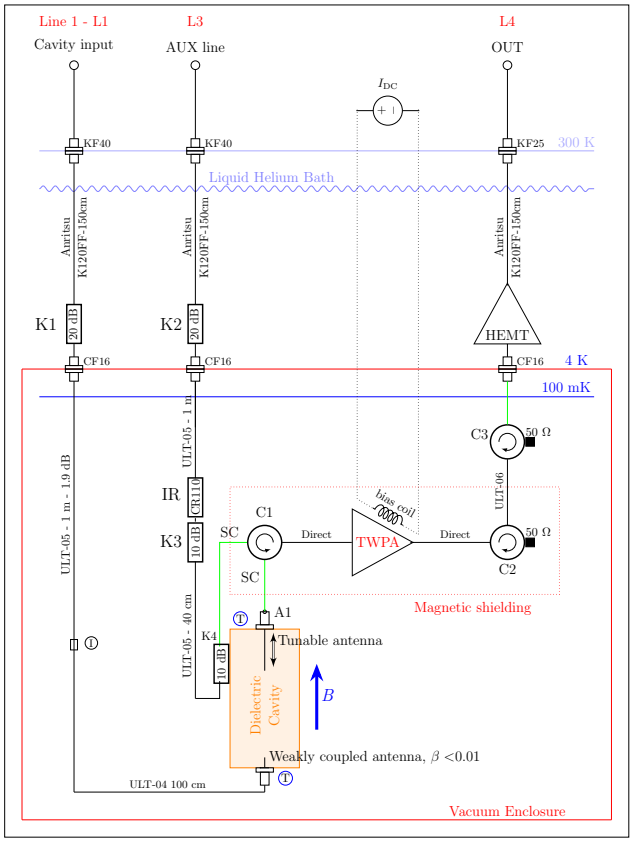

(a) Electronic schema of the RF Cryogenic layout, divided in the three temperature levels, namely 100 mK, 4 K and T_{He}

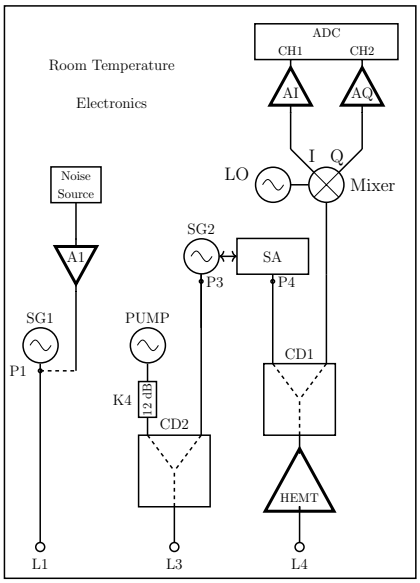

(b) Room temperature electronics schema: this apparatus is connected to the one on the left by means of the switch circuit

Figure 3.6

3.3.1 Cryogenic setup

This circuit is responsible for the amplification of the signal from the cavity to the room temperature detection devices. It is mainly comprised of the following components: a Traveling Wave Parametric Amplifier (TWPA), a High Electron Mobility Transistor (HEMT), three circulators Ci, some attenuators, two antennas and finally a wide set of cables connecting them. The setup is divided in three main stages, depending on their temperature, which can be 100 mK, 4 K or T_{He}, temperature of the liquid helium. I will briefly describe the comprising component's working principle in this Section, while a complete description of the TWPA functioning will be given in Section 3.4. Names and the connections between components of this Section follow the graphical description given in Figure 3.6a.

The **HEMT** amplifier is a type of field-effect transistor (FET) widely used in high-frequency, low noise, and high gain experiments. The HEMT operates based on the principle of high electron mobility in a junction between two semiconductor layers with different bandgaps. At the interface of these two materials, a two-dimensional electron gas (2DEG) forms due to the difference in bandgaps: this constraints electrons to a very thin layer. This 2DEG is characterized by high electron mobility owing to the high purity of the semiconductor crystal. The working principle of a HEMT is the following: a voltage applied to the gate terminal allows to control the electron flow through the 2DEG. In particular the gate voltage modulates the density of the 2DEG, thereby controlling the current flow between the source and drain terminals. Due to the high electron mobility, the HEMT has faster switching times and lower noise: thus it can operate at very high frequencies, and in particular in the range of GHz we are interested in, with minimal signal degradation. These devices are able to reach a noise temperature of $T_n \sim 4$ K while amplifying the signal of $30 - 40$ dB in a frequency range of even 6 GHz[41].

The **microwave circulator** is a non-reciprocal passive device that aims to channel the direction of signal flow among multiple ports. In a three-port circulator, signals are forced to flow from port 1 to port 2, from port 2 to port 3, and from port 3 back to port 1, in a unidirectional manner. The working principle relies on electromagnetic wave propagation and magnetism: in the inner part of the circulator lies a ferrite material placed in a magnetic field, which causes the material to exhibit non-reciprocal properties. When a microwave signal enters the circulator, the ferrite material, influenced by the external magnetic field, creates a rotating magnetic field within the device. This rotating field interacts with the electromagnetic wave, effectively guiding it to the next port in the sequence.
A microwave circulator, like C1 in Figure 3.6a, is crucial in systems that require the separation of transmitted and received signals using the same antenna: in fact it can direct the transmitted signal coming from line L3 to the antenna A1 while simultaneously routing the received signal to line L4 for processing, without interference. Two other circulators, namely C2 and C3, are essential for the isolation of

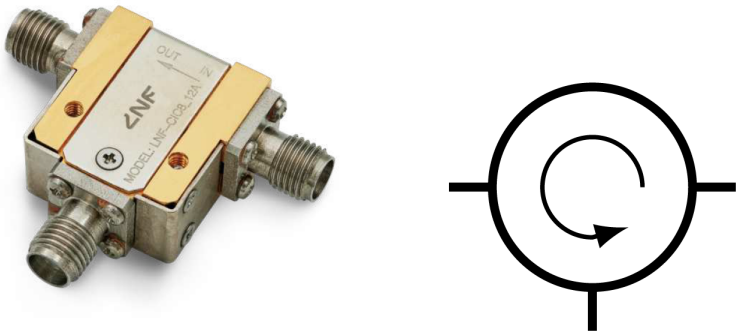

(a) (b)

Figure 3.7: Photo of a circulator (a) and typical circuit scheme symbol (b)

the 100 K stage from electronic noise coming from the HEMT: signals that could be injected back into the line are thermally dissipated on a $50\,\Omega$ resistance, while signals following the inverse path do not encounter this dissipation.

In order to ensure the cryogenic temperature reach, a wide set of **attenuators** is placed on line L1 and L3. In coaxial cables, in fact, thermal photons coming from higher temperature regions can enter the lower temperature ones: attenuators are therefore essential to stop thermal photons from passing. An attenuator at stage i with attenuation A_i is able to reduce the noise photon occupation number $n_i(\omega)$ according to the formula:

$$n_i(\omega) = \frac{n_{i-1}(\omega)}{A_i} + \frac{A_i - 1}{A_i} n_{BE}(T_{\text{att},i}, \omega) \tag{3.3}$$

where n_{i-1} is the noise photon occupation number at the previous stage and $n_{BE}(T_{\text{att},i}, \omega)$ is the average number of photons per mode ω at thermal equilibrium at the attenuator temperature $T_{\text{att},i}$. This quantity is defined from the Bose Einstein distribution:

$$n_{BE}(T_{\text{att},i}, \omega) = \frac{1}{e^{\frac{\hbar\omega}{k_B T_{\text{att},i}}} - 1} \tag{3.4}$$

Two last components worth mentioning are the two **antennas** A1 and A2. The first one is a tunable antenna, that we can move using another stepper motor at room temperature, whose working principle is the same used for the cavity aperture. It is crucial for this antenna to reach both the overcoupled regime, since a coupling factor $\beta = 2$ is required during the measure in order to maximize the scan rate, and the critical regime with $\beta = 1$ in order to evaluate the cavity properties. The second antenna, positioned on the bottom of the cavity, is fixed and undercoupled, with a coupling factor $\beta \ll 1$.

3.3.2 Room Temperature setup

The room temperature setup is located in the acquisition station and the instrument it is comprised of, as shown in Figure 3.6b, are: a Signal Generator (SG1) and a Noise Source (NS) connected to line L1, a Pump, and another Signal Generator (SG2) are connected to line L3 and finally a Spectrum Vector Analyzer (SVA), a Mixer, a Local Oscillator (LO), two filters and the Analog to Digital Converter (ADC) are connected to line L4.

The **Signal Generators** are devices used to produce electrical signals with varying waveforms, frequencies, and amplitudes: in our setup they are used for testing and debugging the cryogenic setup. It works by generating a stable and precise output signal, which can be configured as sine, square, triangle, or other complex waveforms, and with a variable frequency: in particular it is important for its ability to generate signals at different precise frequencies. For the goals of our experiment, the SA connects to one of them in a master-slave connection and uses it as input signal in lines L1 and L3. Another SG is used as a reference for the data acquisition: a signal of fixed power and frequency is injected from line L1 during the experiment. This last signal will be referred as "reference peak", since it is expected not to change its power and frequency over time, and is used to track the gain changes during the data acquisition.

The **Spectrum Vector Analizer** is used to measure and analyse the frequency spectrum of electrical signals, providing measurements of the signal's amplitude, phase, and frequency characteristics. This is a better instrument with respect to a basic spectrum analyzer, since the latter only measures the magnitude of signals across a frequency range. Our SVA is in fact better, since it can perform a complex signal analysis, which is invaluable for the design and test of our experimental setup. The working principle of the SVA involves mixing the input signal with a local oscillator (LO) to convert the signal to a lower intermediate frequency (IF), where it can be more easily processed. This process allows the analyzer to cover a wide range of frequencies with high precision. The vector aspect of the analyzer comes from its ability to decompose the signal into its in-phase (I) and quadrature (Q) components, which represent the signal in a complex plane. Thanks to this conversion, the SVA is able to measure both the amplitude and phase of each frequency component within the signal.

The **Local Oscillator** is able to generate a stable and precise periodic signal at a specific frequency: this reference signal is used to mix with incoming signals to produce intermediate frequencies (IF). Local oscillators are usually the most stable electronic devices, and are therefore used also as a reference for the frequency by other devices.

The **Mixer** is the device responsible for the down-conversion of the electronic signal, which in the present case entails conversion from about 10 GHz to a few MHz. The

mixer, thanks to its nonlinear characteristics, takes as input the radio frequency and local oscillator signals, with frequency f_{RF} and f_{LO} respectively, and give in output signals at frequencies $f_{RF} + f_{LO}$ and $f_{RF} - f_{LO}$. The sum is discarded, while the difference, known as the intermediate frequency (IF), is kept for further processing. This down-conversion is particularly important for the following procedures, given the higher reliability of electronic components for lower frequencies, and for the data saving, since we can sample the signal at lower frequencies and therefore reduce the data to store by a factor 2000.

The **low-pass Filters** are electronic passive components that suppress all the signals at higher frequencies. In our case, once the signal is down-converted, two low-pass filters with a passband of 1.7 MHz are inserted in the line L4, just before the signal digitalization. In particular our filter is a 8-poles filter, which means that, even for signals that are slightly above the passband frequency, the suppression is -160 dB per decade.

The **Analog to Digital Converter** is the device responsible for converting continuous analog signals into discrete digital values. In the ADC an analog signal is sampled at regular intervals of time and each sample is quantized into a corresponding digital value. The precision of this conversion is determined by the resolution of the ADC itself, that in our case is expressed in terms of 16 bits. The possible discrete values are in the range $[-2^{15} : 2^{15} - 1]$, corresponding to the voltage values $[-1 : 1]$ V: for an higher precision, input signals are calibrated so that signals entering the ADC cover the widest possible voltage range.

3.3.3 Switches

A set of switches is placed between the cryogenic environment and the room temperature electronics: these components aim to connect the correct cryogenic line to the correct room temperature one. Thanks to the introduction of these switches, we are able to perform measurements without connecting and disconnecting cables once the experiment is running, resulting in a much higher reliability of the results.

3.4 Travelling Wave Parametric Amplifier (TWPA)

Traveling Wave Parametric Amplifiers (TWPAs) are crucial components in the field of quantum information processing. As said in equation 3.2, the first stage of the amplification chain is the most important: it has to introduce the smallest amount of noise and the highest possible gain in the widest allowed frequency region. TWPAs are able to trade-off these requirements and represent the best-known fit as first stage of the amplification chain.

The most important parameter for the required amplifier is the ability to provide amplification with minimal added noise. TWPAs are then particularly valued since

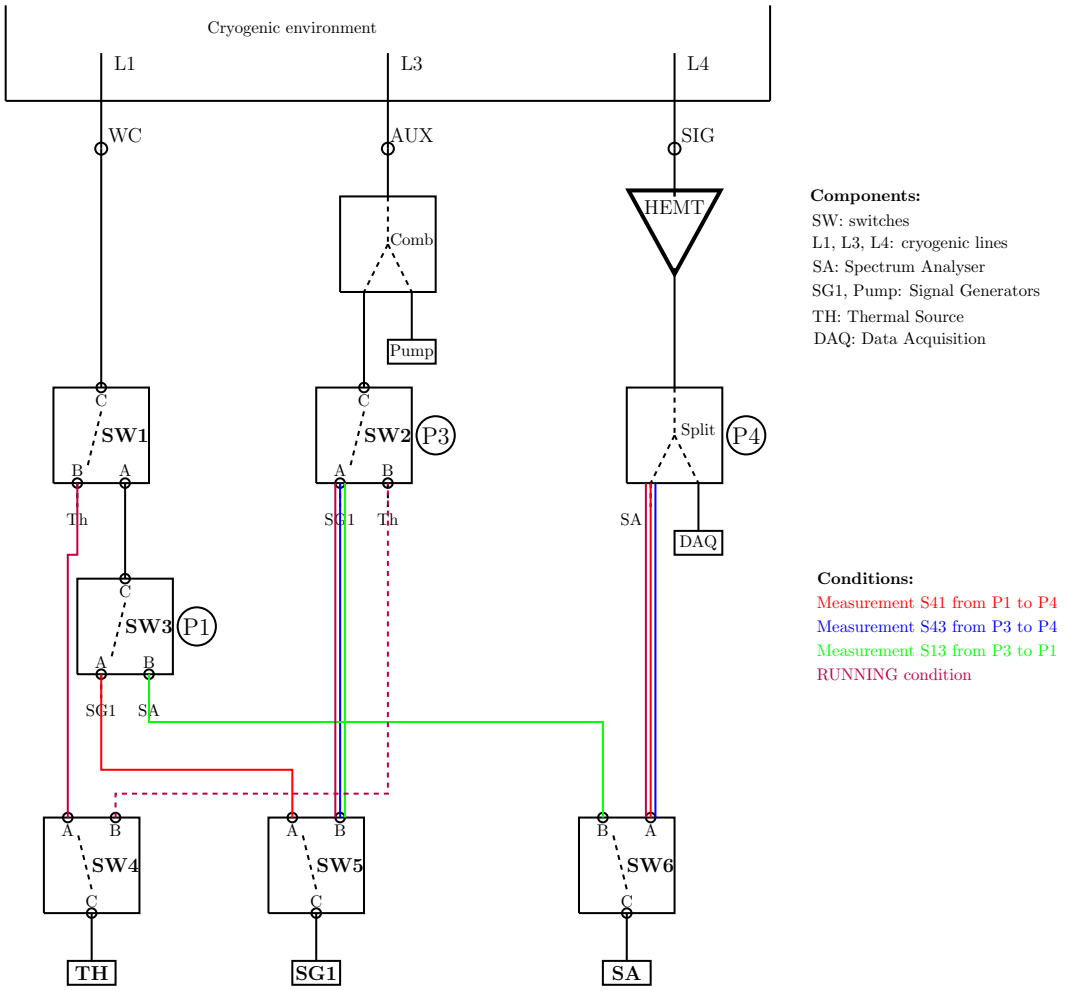

Figure 3.8: Schema for the switches circuit, connecting the cryogenic environment (top) to the room temperature electronics (bottom). Different colors define different configurations used for the calibration of the cryogenic experimental apparatus.

they can introduce the minimum level of quantum noise, usually called Standard Quantum Limit (SQL). This device noise temperature is evaluated to be around 0.6 K, which allowed to reach a noise temperature of [1.2 : 1.6] K at the cavity level during the experiment.

As an amplifier another key characteristic is to increase the power of an input signal, ideally without introducing significant distortion: the gain is therefore another important parameter. It is defined as the ratio between output and input signal amplitude and denoted as $G(\omega_s)$, given its dependence on the signal frequency. In Figure 3.9a the gain profile of the TWPA used in the present work is shown.

Given the haloscope requirement to probe for wide frequency regions, another important parameter is the bandwidth, defined as the frequency range over which the gain remains above a certain threshold, which is usually $G_{\max}/2$ in linear units or $G_{\max} - 3\,\mathrm{dB}$ in logarithmic units. Other devices, such as Josephson Parametric Amplifiers (JPA), can still reach noise temperatures at the SQL and have gains up to 40 dB, but the TWPA can ensure this reach for a bandwidth more than 4 GHz wide.

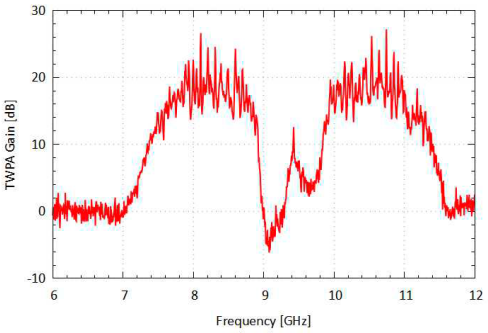

(a) TWPA gain profile presenting the two amplifications for signal and idler

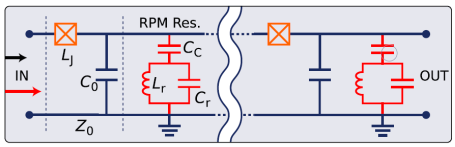

(b) JTWPA amplificator

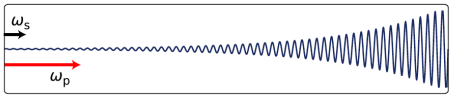

(c) Gain along the JJ chain

Figure 3.9: TWPA characteristics: (a) Broad band gain profile for the TWPA at a fixed working point, after the subtraction of the passive losses (b) Simplified circuit representation of a Josephson Traveling Wave Parametric Amplifier (JTWPA) where the phase-match amplification process is governed by the LC circuits (in red) and each Josephson Junctions inductors L_J and shunted capacitances C_0 (c) Signal amplification along the transmission line [42]

3.4.1 Traveling Wave Amplification Mechanism

Parametric amplification in TWPAs arises from nonlinear interactions within the medium through which the signal travels. These interactions are typically modeled using the concept of wave mixing, which can occur through either three-wave mixing (3WM) or four-wave mixing (4WM). In three-wave mixing, a high-frequency pump wave at frequency ω_p interacts with a signal wave at frequency ω_s, generating an idler wave at a difference frequency $\omega_i = \omega_p - \omega_s$. This process conserves energy by transferring it from the pump to the signal and idler waves, effectively amplifying the signal. Four-wave mixing, on the other hand, involves the interaction of two pump photons with a signal photon, creating an idler photon while conserving the total energy: $2\omega_p = \omega_s + \omega_i$. As the previous process, 4WM results in the amplification of the signal, but occurs in media with third-order nonlinearities. In Figure 3.9a are visible two maxima in the gain profile in correspondence of the frequency of signal and idler: the pump frequency is set to be in the minimum in between.

The distinguishing feature of a TWPA is its use of a traveling wave structure, where the signal, pump, and idler waves propagate together along a nonlinear transmission line, such as one based on a Josephson junction array, as the one presented in Figure 3.9b. Unlike parametric resonant amplifiers, which have bandwidth constraints due to the presence of the cavity in their circuit scheme, TWPAs offer a broadband amplification. In a TWPA, the gain is achieved by the continuous interaction of the signal with the pump wave over a long distance, allowing for a cumulative amplification effect: the idea is graphically introduced in Figure 3.9c. The phase matching between the signal, pump, and idler waves is critical for maintaining efficient energy transfer throughout the amplifier's length. The nonlinear properties of the transmission line, typically enhanced by the use of superconducting materials, allow for strong amplification over a wide frequency range, with gains often exceeding 20 dB and bandwidths extending over several gigahertz. As visible from the spectral gain shape in Figure 3.9a, gain ripples are present in the working region. For axion search, due to the reduced cavity linewidth, the presence of these ripples does not characterize a problem: the TWPA electronic inputs can be changed in order to work on a gain local maximum, whose gain does not consistently change in the selected frequency region.

3.4.2 Preparation of the TWPA

The efficiency in the matching between pump and signal photons is determined by three parameters: the bias flux, which is controlled by the DC current through a superconducting coil, which changes the input signals amplification along the many JJs, and the pump amplitude and frequency. It is then important to change these three parameters each time the scanned frequency is modified, in order to optimize the TWPA performances for that specific frequency range.

A preliminary value of the bias current is given by the constructor, in our case it was set to $I_{DC} = 1.3$ mA: the optimization mainly involves the pump frequency and amplitude setting. The pump frequency in fact is not fixed by design in a reversed Kerr TWPA, allowing flexibility in matching it to the signal frequency of interest: the characteristic TWPA gain profile exhibits two lobes, with many gain ripples as one can see in Figure 3.9a, and the pump frequency is usually chosen so that the signal frequency is within one of these gain maxima. The pump amplitude is then optimized to achieve maximum gain without driving the TWPA to saturation. This is done by gradually increasing the pump power until the gain reaches a plateau, indicating the onset of saturation, and then reducing it slightly to maintain linear operation with an high gain. A slight adjustment of the bias current, usually of the order of $10\,\mu$A, along with the other parameters, can be performed in order to further increase the gain within the non-saturating region. The optimization process ends when, in a non-saturating region, the maximum gain, that in our case was around $20 - 22$ dB on average, is reached: the unpredictable behaviour of the gain w.r.t. the choice of these parameters causes this optimization not to be automatable.

At each cavity frequency that we set, i.e. at each resting point in the cavity aperture, the TWPA performances, namely the gain and the temperature noise, need to be monitored. In the frequency range probed in the present thesis, which is approximatively 15 MHz, small adjustments of the parameters were done at each step: the usual change was about 10 μA for the bias current, 300 kHz for the pump frequency, corresponding to the cavity frequency shift, and 0.1 dB for the pump amplitude. Sometimes, due to the small cavity frequency shift w.r.t. the TWPA region corresponding to the maximum gain, these parameters were kept unchanged.

3.5 Noise Temperature

Noise temperature is a measure of the noise power introduced by an amplifier relative to the thermal noise at a given temperature, as described in Section 2.5. For any new TWPA working point corresponding to a different cavity aperture, once the TWPA is correctly operational, it is possible to proceed with the measurement of both gain and noise temperature of the receiver chain with the method described in the following.

The idea is to use a Signal Generator (SG) to inject calibrated signals in lines L1 and L3, as defined in Section 3.3, and measuring the output spectra at points P1 and P4 with the Spectrum Analyzer (SA). The procedure, fully described in [43], allows to measure the noise temperature at the cavity output, without the need of switches at cryogenic temperature or calibrated noise sources. It involves the measurement of three transmission power spectra: from point P1 to point P4 (S41), from point P3 to point P4 (S43) and finally from point P3 to point P1 (S13). To minimize errors on both gain and noise temperature, we inject a few values of input power far from the saturation point[42]. Using a linear regression for these detected powers, an estimation of the three gain lines is obtained: g_1 from point P1 to antenna A1, g_3 from point P3 to antenna A1 and g_4 from antenna A1 to point P4. All the measurements of this kind are performed at the resonating frequency if in transmission, otherwise a slightly detuned frequency is used. The important quantity for the experiment's purpose is g_4, since it represents the gain from the antenna to the data acquisition electronics, which is the complete detection chain's gain.

From g_4 one can then evaluate the equivalent system noise temperature T_{sys} of the detection chain at point A1, thanks to spectra S41 and S43, and their relation:

$$P_n^{xy} = g_4 k_B T_{sys} B + \text{Noise}_{SA} \qquad (xy) = \{14, 34\} \tag{3.5}$$

where k_B is Boltzmann's constant, B is the SA's resolution bandwidth and Noise_{SA} is the SA's noise, which is of the order of hundreds of fW, being negligible in these kind of measures.

3.6 Fano Interference

Fano interference is typically observed in wave scattering experiments when a resonantly scattered signal interferes with background paths, such as port-to-port leakage, impedance mismatches, or other device imperfections. In microwave resonator measurement setups, these background paths are inherently present, and the finite circulator isolation is a dominant source of background interference. In our experiment the presence of signals different from the expected ones forces the study of these phenomena.

In single-port reflection measurements, the measured signal S_{11}^{Σ} is given by the interference between a part of the reflected signal and the scattered signal. This phenomenon is briefly shown in Figure 3.10(b) for the reflection of the signal, but a similar phenomenon can occur also in the case of a transmitted signal, as shown in Figure 3.10(c). In both the cases it can can be expressed in the complex phasor language as:

$$\begin{cases} \text{Reflected:} & S_{11}^{\Sigma} = (1-b)S_{11} + be^{i\varphi} \\ \text{Transmitted:} & S_{21}^{\Sigma} = (1-b)S_{21} + be^{i\varphi} \end{cases} \tag{3.6}$$

where b and ϕ are respectively the amplitude and the phase of the background path relative to the resonant signal. This interference can result in systematic distortions of the resonator response, making it difficult to extract an accurate value for the internal quality factor. Away from resonance, the reflection coefficient S_{11} equals unity, but the measured baseline $|S_{11}^{\Sigma}|$ oscillates by $\pm b$ as a function of φ, which depends on the optical path length between the interfering signals.

The presence of Fano interference is a major phenomenon in hanger-type transmission measurements, i.e. where three cables are connected together in a T-junction without the presence of a circulator. Here the two-port crosstalk gives rise to the leakage signal $be^{i\varphi}$. Even with the insertion of a circulator, the resulting amplitude lineshapes show dips and peaks at various degrees of asymmetry depending on the relative background phase φ, as can be seen in 3.10(d, e). It is important to underline that measuring a symmetric lineshape is no guarantee for the absence of Fano interference. For instance, in hanger-type transmission measurements, asymmetric amplitude lineshapes are commonly interpreted as a result of impedance mismatches, but their absence doesn't assure a correct impedance match.

For the purposes of this thesis, a typical resonating process with a dephasing contribute is described via a typical Fano function for a lossy two-port system [44]:

$$f(\omega) = t_d^2 \cdot \frac{\left(q + \frac{\omega-\omega_0}{\gamma}\right)^2}{1 + \left(\frac{\omega-\omega_0}{\gamma}\right)^2} + \alpha \tag{3.7}$$

where t_d is the amplitude, ω_0 is the resonating frequency, γ is the frequency width of the resonance, α is the offset and q is the shape factor describing the interference between the resonant and non-resonant scattering pathways. This latter parameter is very important for the correct shape of the figure, since it quantifies the amplitude asymmetry of the signal: it is therefore directly connected with the interference phase φ, as presented in Figure 3.10(e). Three discrete values of q are worth mentioning: $q = 0$ corresponds to a deep (green in Figure), $q = 1$ corresponds to a perfectly asymmetric function (blue in Figure) and finally $q \to \infty$ corresponds to a peak (red in Figure). To these three conditions are connected the relative dephasing of the signal: $\varphi = 0, \pi/2, \pi$ respectively.
Equation 3.7 is the fitting function we are going to use in this work to interpret and estimate any resonating process, and in particular, their power spectra. Due to physical conditions, some simplification of the formula can be made: for a signal that is transmitted through the cavity, we can assume that no dephase occurs, leading to the imposition of $q \to \infty$, which corresponds to a Lorentzian profile. On the other hand, for a signal that is reflected at the entrance of the cavity, we can assume that an opposite phase is introduced, corresponding to the imposition of $q = 0$ in the Fano formula.
Unluckily for us, these simplifications can not be used, since even a small impedance mismatch can affect the fit, introducing systematic errors in the parameters of interest: furthermore, for a complete description of the reflection signal, one must take into account also the coupling with the antennas.

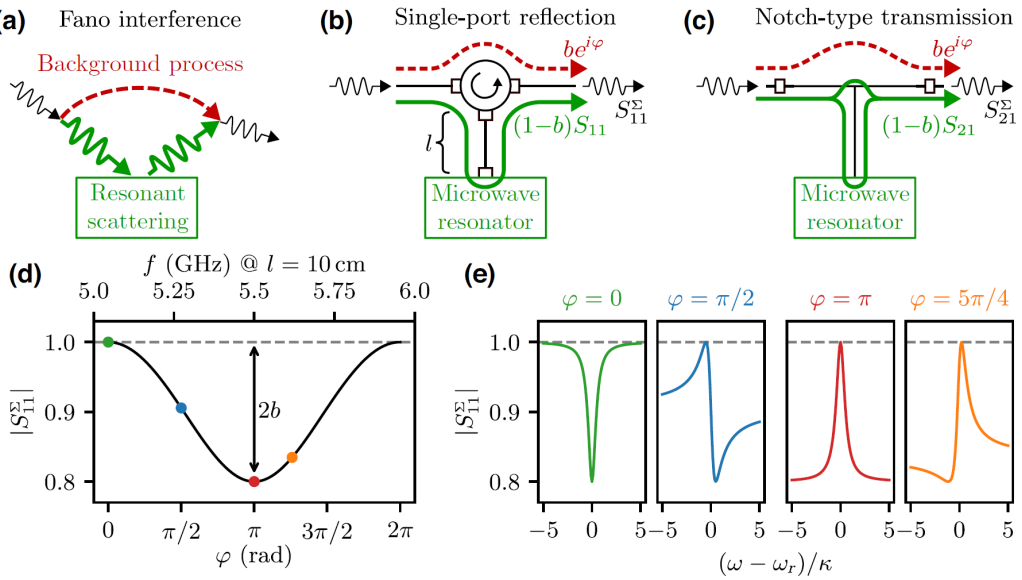

Figure 3.10: Origin and symptoms of Fano interference in microwave resonator measurements. (a) Schematic depiction of Fano interference in wave scattering experiments. (b) Single-port reflection measurements where finite circulator isolation constitutes a dominant background path. (c) Hanger-type transmission measurements with two-port crosstalk. (d) Background interference pattern showing amplitude oscillations as a function of the interference phase φ and (e) resulting Fano figure. [45]

Chapter 4

Data acquisition and analysis

In this last Chapter, will briefly describe the data acquisition procedure for an haloscope experiment, and in particular the one followed during the May-June 2024 QUAX$_{a\gamma}$ run. The data acquisition process can be divided into the following procedural steps:

- preventive controls before the run: mainly check that the electronic components do not introduce distortions to the final power signal;
- a number of steps are done with the positioner, sufficient to shift the cavity frequency of a quantity comparable to a linewidth (around 300 kHz);
- the cavity transmission and reflection spectra are recorded;
- optimization of the TWPA gain as described in detail in Section 3.4.2;
- noise temperature evaluation as detailed in Section 3.5;
- acquisition of a spectrum with noise generated by a thermal source input from line L1 to the cavity, as shown in Figure 3.6b;
- scientific data taking, with a live output of the acquired spectrum;
- control of the cavity temperature;
- data upload on the cloud.

The data analysis procedure is inspired by the analysis introduced by the HAYSTAC experiment[46], applicable to data acquired with a detector bandwidth that is much larger than the linewidth of the searched signal $Q_c \ll Q_a$. An example of analysis devised for experiments with cavity quality factor comparable or larger than Q_a is reported in [47]. The performed analysis will follow the steps:

1. Use the cavity reflection and transmission spectra to identify possible compromised runs, that will be excluded from further analysis;

2. Evaluate the spectra for each run, combining the signals in phase and quadrature for each run. Correct then the spectra taking into account the frequency dependence of the TWPA gain and the filters' effect; finally, using the reference peak information, compensate for the gain behaviour over time;

3. Average together all raw spectra aligned according to IF frequency, in order to spot compromised IF bins, which will be cut from further analysis. Divide then each run into smaller chunks and fit the spectrum shape retrieving the expected cavity frequency, then use this behaviour to spot cavity frequency shifts: runs that experience a shift in the cavity frequency are divided accordingly;

4. Divide each spectrum by the average baseline and use a Savitzky-Golay(SG) filter to remove the spectral structure in each normalized distribution, then subtract 1. The obtained processed spectra are dimensionless and described by Gaussian statistics;

5. Divide each spectrum by the axion conversion power and multiply them by the average noise, in order to obtain a set of *rescaled spectra*. Then combine them together, aligning them by the RF frequency and taking the optimally weighted sum bin per bin, obtaining the *combined spectrum*;

6. Use a weighted average of adjacent bins to rebin the combined spectrum, obtaining the *grand spectrum*;

7. Set a threshold on the SNR of the grand spectrum: all bins exceeding this threshold are flagged as axion candidates.

For all the axion candidates, a rescan at that specific frequency is needed: after the candidate has been excluded, the grand spectrum is used to evaluate an upper limit on the coupling constant $g_{a\gamma\gamma}$.

4.1 Data acquisition

In this Section we will briefly describe the data acquisition procedure followed during the May-June 2024 QUAX$_{a\gamma}$ run following the steps described in the preface of this Chapter. The experimental procedure to run the QUAX experiment is partly automated as the data acquisition procedure is well known. Thanks to the switches presence, the data acquisition is highly automated and in particular three main programs have been written: one for the evaluation of the noise temperature (NTp), one for the data taking procedure and saving (DTp) and finally one for the cavity transmission and reflection spectra acquisition (SAp). Other steps, as the TWPA optimization and the cavity tuning, still have to be performed by an operator: these actions are difficult to automatize for their non-linear nature and the unpredictable behaviour that we described in Sections 3.4.2 and 3.2.1 respectively. As a consequence of this, also LO and reference frequency have to be set by hand.

4.1.1 Cavity tuning and control

As a first step in the run procedure, we need to tune the cavity to the correct frequency: as a trade-off between sensitivity and gain time, we decide to acquire at intervals of one linewidth for cavity frequency. This means that in principle we want to move of exactly a FWHM from one measure to the following one: in particular, for a cavity frequency of $\nu_c \sim 10$ GHz and a loaded quality factor in the range $Q_L \in [30000 : 50000]$, one linewidth is expected to be in the range $\Delta\nu \in [200 : 333]$ kHz. The stepper allows to tune the cavity of up to the desired quantity, but it is not reliable in the shift, as previously described in Section 3.2.1.

After the operator has completed the frequency change, cavity spectra in transmission and reflection are acquired. In the spectra acquisition program (SAp), the procedure is as follows:

- For the **transmission**, a -10 dBm input is injected from line L1 and detected from line L4: transmission spectrum is therefore named S14. The SVA preliminarily sweeps in the expected frequency range and takes the maximum power value as the approximate value of the cavity frequency: then it scans for the frequencies in a 2 MHz range centred in the approximative central frequency and acquires it with a 25 kHz resolution.
- For the **reflection**, a -15 dBm is injected from line L3 and detected from line L4. Similarly to the transmission procedure, the spectrum S34 recorded at the SVA is first used to identify the minimum power position for reflection as the cavity frequency: thus reset the instrument parameters to get a centred spectrum with the same 5 MHz resolution.

Once the cavity frequency is known with a precision at the order of kHz, the LO frequency is set 1 MHz below the cavity one. Similarly the reference peak is set 0.2 MHz below the LO frequency:

$$f_{\mathrm{LO}} \sim f_c - 1\mathrm{MHz} \qquad f_{\mathrm{ref}} = f_{\mathrm{LO}} - 0.2\mathrm{MHz} \tag{4.1}$$

The ADC samples at a rate of $f_{\mathrm{ADC}} = 4.4$ MHz, thus the maximum signal frequency range is $[-2.2 : 2.2]$ MHz according to the Nyquist-Shannon theorem[48]: therefore it is reasonable to set the difference between LO and the cavity frequency at 1 MHz for its centrality in the positive range. The reference peak position has indeed been chosen such that it is out of the cavity influence, but not enough to behave differently w.r.t. the cavity for what concerns the TWPA performances over time.

4.1.2 Thermal and actual run

Once the TWPA is optimized for the current cavity frequency, the noise temperature program (NTp) can be launched. Then a 10000K noise source, whose output noise

is amplified to compensate for the input lines loss, is switched on and the output signal is fed to the mixer-ADC line: the data taking program (DTp) is now run.
The DTp acquires the ADC output as a time series: these data can be converted in the frequency space[1] and allow for a better estimation of the loaded quality factor and the cavity frequency, since the Signal to Noise Ratio (SNR) in the frequency domain is much higher than the one retrieved in the previous acquisitions.
The acquisition time for this step is of approximatively 19 seconds: for a more precise signal we should acquire data for a longer amount of time, but these 19 seconds are sufficient for the detection of possible problems: in fact, during this run, a rough analysis of the spectrum is shown on the computer and, most of the times, we are able to spot errors. These runs will be referred as "Thermal" runs in the following of this thesis, due to the presence of the thermal source.

The thermal source is then switched off and the DTp is launched again: the system automatically records a number of spectra decided by the operator based on the required SNR, as we recall from equation 2.50. In addition, the available liquid helium or the availability of data taken in the same region need also be considered for the correct integration time estimation. In the May 2024 run, we collected data for $1900, 3800, 7600, 15200$ or 19000 seconds, based on the previously mentioned parameters, while in the June 2024 run, we restricted this choice between 3800 and 19000 seconds. These runs will be referred as "Vacuum" runs in the following of this thesis, due to the absence of inputs in the cavity: the signal coming from it is expected to be only due to axion conversion.
Also during this run, for the sake of comprehension of the experiment behaviour, a primary analysis is performed under-sampling the raw data. When errors occur, usually the run is interrupted and the data are conserved until the error occurrence.

4.1.3 Data stream and saving

The acquired data, which is the time series of ADC output, are divided into files containing 2^{23} samples and saved locally. Each sample is comprised of both the in-phase component and the quadrature one: the dimension of each of them is $l_d = 2$ bytes $= 16$ bits. Thus the total dimension of each file is approximatively $M_{\text{file}} \sim 33.6$ MB. The ADC is also sampling at a fixed frequency $f_{\text{ADC}} = 4.4$ MHz, which means that every second it is able to acquire $4.4 \cdot 10^6$ samples: each saved file corresponds then to $t_{\text{file}} = 1.9$ s[2] of run. The incoming data are then saved in binary files locally and, after the completion of a single run, both the thermal and the actual data are uploaded on the cloud: binary files are then saved for future analysis and no data is thrown away.

[1] This procedure can be easily performed using the Fast Fourier Transform (FFT) algorithm, that will be further discussed in Section 4.3. For the purpose of this Chapter, we only need to know that the time series acquired with the ADC can be transformed back to the frequency space.

[2] The time needed for a single run has been determined by the number of such saved files

The entire data acquisition process for the May-June 2024 runs covered a total range of 15 MHz, considering a two-linewidth frequency region per run, divided in three main frequency regions, for a total of approximatively 4.9 TB.

4.2 Cavity behaviour

As a first analysis, we need to know the cavity characteristics: a fit has been performed on the reflection and transmission spectra, in order to have more reliable parameters. The expected power spectrum shape can be retrieved by the Fano formula, as described in Section 3.6, imposing the shape factor q to infinity for the transmission and equal to zero for the reflection, leading to the following results:

- The transmitted power expected profile follows a Lorentzian function centered in the cavity frequency $f_0 = f_c$:

$$T(f; A, \Gamma) = L(f) = A \frac{\Gamma/2}{(f - f_0)^2 + (\Gamma/2)^2} \tag{4.2}$$

  where A is the intensity nearby the maximum, Γ is the FWHM (Full Width at Half Maximum) and f_0 is the frequency relative to the peak. Thus Q_L, being a quality factor, corresponds to the ratio between signal peak frequency f_0 and its FWHM:

$$Q_L = \frac{f_0}{\Gamma} \tag{4.3}$$

- The expected profile for the power reflected on the cavity is given by the following function [49], with the minimum corresponding to the cavity absorption, which occurr at resonance, meaning at the cavity frequency $f_0 = f_c$:

$$R\left(f; A, \beta, Q_0\right) = A \frac{(\beta - 1)^2 + \left(Q_0 \left(\frac{f}{f_0} - \frac{f_0}{f}\right)\right)^2}{(\beta + 1)^2 + \left(Q_0 \left(\frac{f}{f_0} - \frac{f_0}{f}\right)\right)^2} \tag{4.4}$$

  where A is the intensity of the background and both the antenna coupling factor β and the cavity quality factor Q_0 are made explicit.

As the spectra in transmission and reflection are not fitted by the functions 4.2 e 4.4, we have to take into account possible mismatches due to the utilization of a circulator, see Section 3.6. The acquired spectra are then fitted by:

$$T\left(f; A, \Gamma, q\right) = \left| \frac{A}{\Gamma/2 - i(f - f_0)} - iq \right|^2 \tag{4.5}$$

$$R\left(f; A, \beta, Q_0, q\right) = \left| A \frac{\beta - 1 + iQ_0 \left(\frac{f}{f_0} - \frac{f_0}{f}\right)}{\beta + 1 + Q_0 \left(\frac{f}{f_0} - \frac{f_0}{f}\right)} - iq \right|^2 \tag{4.6}$$

An example of the reflected and transmitted power spectra is presented in Figure 4.1 with the relative fit. For the transmission the Lorentzian fit is presented: giving a justification in the introduction of the q parameter.

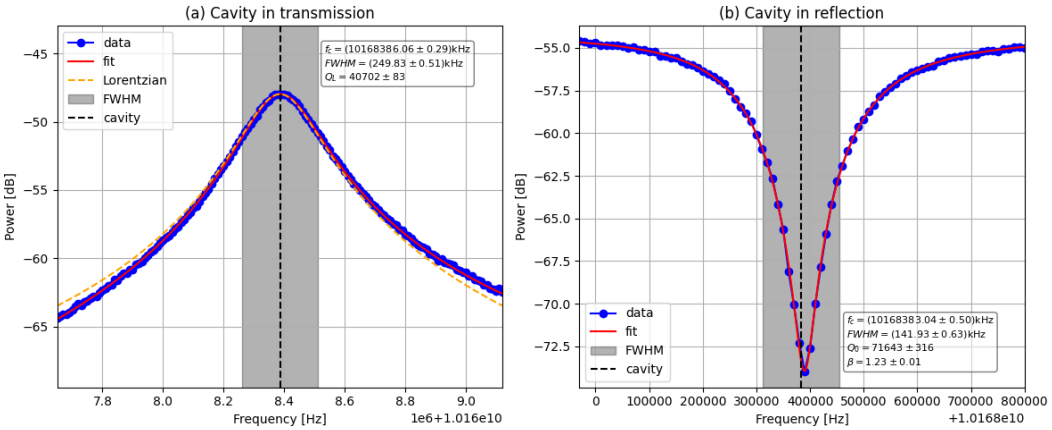

Figure 4.1: Measures in transmission (a) and in reflection (b) for run 655 with respective fit and estimated parameters

In Figure 4.2 we compare the values of loaded quality factor Q_L and the cavity resonance frequency f_c obtained by fitting with eq 4.5 and 4.6 respectively the data in transmission and reflection, acquired during the whole QUAX$_{a\gamma}$ run. The coupling coefficient β from fits in reflection, still coming from equation 4.6, is shown in the lower panel. Before judging the results, we must say that the fit errors cannot be trusted, since different initial parameters lead to different results of the fit. In the frequency difference plot, shown in Figure 4.2a, the error bars are the fit errors, much smaller than the discrepancy between the frequencies, which spans across a 20 kHz range approximatively, that can then be taken as the fit resolution.
On the other hand, quality factors do have a different behaviour: even though we can't trust the fit errors, the quality factors evaluated in reflection and transmission cannot be considered compatible, as one can see from Figure 4.2b. One can clearly see that those evaluated in reflection are systematically smaller than the transmission ones: this discrepancy could be explained by an elevated value of the undercoupled antenna w.r.t. the expected value $\beta \ll 1$.

4.3 Power spectra

The next step in the analysis is to build the spectra starting from the in phase I and in quadrature Q signal components; from these we are able to retrieve the complex signal as:

$$C = i\frac{I}{\eta} + Q \cdot \eta \tag{4.7}$$

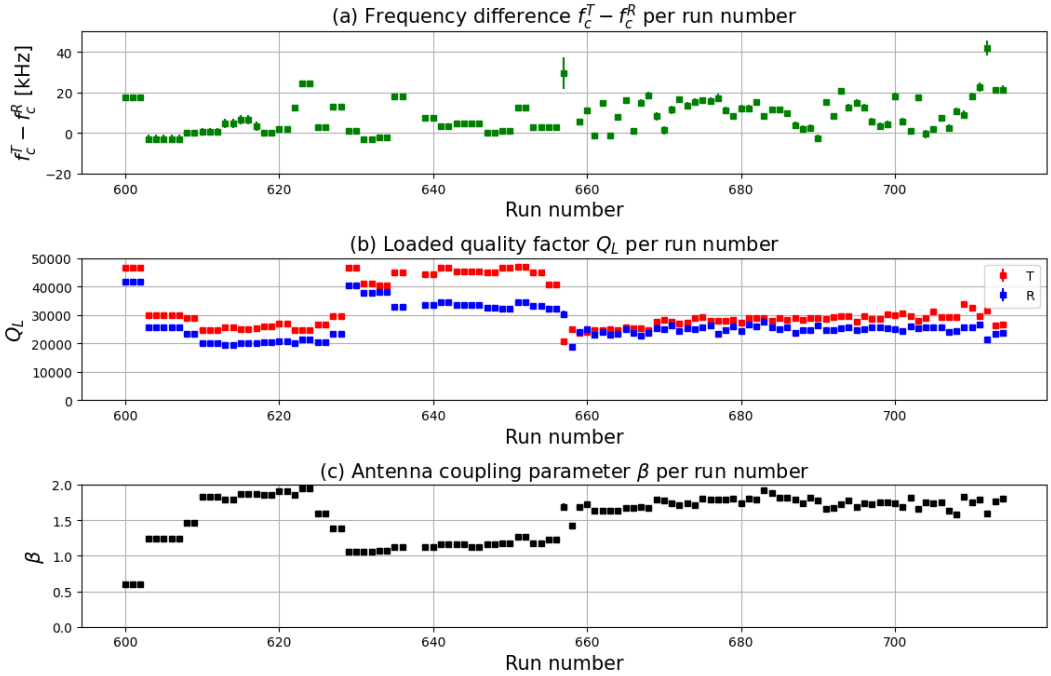

Figure 4.2: Comparison between the parameters of the fits in the transmission and reflection configurations: (a) frequency difference $f_c^T - f_c^R$ and (b) loaded quality factor Q_L. (c) Behaviour of the antenna coupling factor β that explains the oscillations of the quality factor

where i is the imaginary component and η is a correction factor that we have to introduce in order to take into account the different losses on the two channels. The value of η^2 is retrieved experimentally using an amplified thermal source as input; we divide the in-phase component and quadrature one, in order to preserve the norm.

Now we can go from the time domain to the frequency one, but some theoretical clarifications are needed.

4.3.1 Spectral Estimation from Finite-Duration Observations: the Bartlett Method

The power spectrum of a signal provides information about how the signal's power is distributed across different frequency components. The transition to frequency space is important for stationary random processes, since it allows to perform calculations that are faster and easier than the one performed directly on the time signal. In particular, we assume that, in the data acquisition time window, the acquisition process is a stationary process. Under this assumption, if we take the continuous signal $x_c(t)$ with the property of being finite-energy, meaning that $E = \int_{-\infty}^{\infty} |x_c(t)|^2 \, dt < \infty$,

then we can say that, for Parseval's theorem:

$$E = \int_{-\infty}^{\infty} |x_c(t)|^2 \, dt = \int_{-\infty}^{\infty} |X_c(F)|^2 \, dF \tag{4.8}$$

where $X_c(F) = \int_{-\infty}^{\infty} x_c(t) e^{-i2\pi Ft} dt$ is the Fourier Transform of the signal. This particular operation, thanks to the Fast Fourier Transform (FFT) algorithm is much more efficient to be evaluated in the frequency domain. In this Section we want to describe how much this quantity is affected by the presence of a discretized and finite signal, under the assumptions to work with ergodic signals, i.e. signals whose statistical properties can be estimated from a single, sufficiently long realization of the series, and whose properties are consistent across different realizations.

Here, we target the construction of the energy density spectrum of the signal $S_{xx}(F)$ and the autocorrelation function $R_{xx}(\tau)$ defined as:

$$S_{xx}(F) = |X_c(F)|^2 = \left| \int_{-\infty}^{\infty} x_c(t) e^{-i2\pi Ft} dt \right|^2 \tag{4.9}$$

$$R_{xx}(\tau) = \int_{-\infty}^{\infty} x_c^*(t) x_c(t+\tau) dt \tag{4.10}$$

where it is important to note that these two quantities are Fourier Transform pair, since:

$$\int_{-\infty}^{\infty} R_{xx}(\tau) e^{-i2\pi F\tau} d\tau = S_{xx}(F) \tag{4.11}$$

Under the consideration of signal $x_c(t)$ sampled at a constant frequency F_s the sequence $x(t)$ is obtained. The introduced quantities can be rewritten in terms of the discrete signal:

$$R_{xx}(k) = \sum_{n=-\infty}^{\infty} x^*(n) x(n+k) \qquad S_{xx}(f) = \sum_{k=-\infty}^{\infty} R_{xx}(k) e^{-i2\pi kf} \tag{4.12}$$

where k and f are the discretized variables for space x and frequency F.

Now, in a real case scenario, the introduced quantities are affected by the finite duration of the signal: this finite nature of the data sequence introduces several complications that can affect the accuracy and reliability of the spectral estimates. The basic problem is that a truncation of the signal in time distorts its spectral content. This distortion, known as spectral leakage, occurs because the truncation introduces discontinuities at the edges of the observation window, which affect the Fourier transform used to estimate the spectrum. In particular, when estimating the power spectrum from a finite-duration observation, the length of the data record significantly influences the quality of the estimated spectrum. Ideally, for stationary signals, whose statistical properties do not change over time, longer data records

yield better spectral estimates. However, in cases where the signal is non-stationary, a long data record might not be appropriate, as the signal's statistical properties might change within the observation period.

To consider the effect of signal finite duration, we assume to observe a signal for a finite time T, leading to a finite-length sequence $x(n)$ of $N = T/F_s$ samples. From this finite series we are able to estimate the power density spectrum via the calculation of the so-called *peridogram*:

$$P_{xx}(f) = \left| \sum_{n=0}^{N-1} x(n) e^{-i2\pi fn} \right|^2 = \frac{1}{N} |X(f)|^2 \tag{4.13}$$

where $X(f)$ is the Discrete Fourier Transform (DFT) of the sequence $x(n)$. However, even though it is an unbiased estimate, the periodogram is a poor estimator since its variance does not vanish for $N \to \infty$.

A commonly used method to reduce variance of the obtained spectral estimate is the **Bartlett method**, in which the original N point data sequence is divided into K non-overlapping data segments of length $M = N/K$. The periodogram is then computed for each segment $x_k(n)$:

$$P_{xx,k}(f) = \frac{1}{M} |X_k(f)|^2 \tag{4.14}$$

where $X_k(f)$ is the DFT of the k-th segment. An estimate of the power spectrum is then obtained by the average of these peridograms:

$$P_{xx,B}(f) = \frac{1}{K} \sum_{k=1}^{K} P_{xx,k}(f) \tag{4.15}$$

which has a reduced variance compared to using a single peridogram.
It is possible to prove that the variance of this estimate is null in the limit $N \to \infty$ due to the averaging process.

It is important to note that the Bartlett method results in a loss of frequency resolution due to the shorter data segments. Since the single periodogram is computed from a segment of length N, the frequency resolution is $\Delta f = \frac{1}{N}$, thus for the Bartlett method $\Delta f_B = \frac{K}{N}$. In general, an increase of parameter K shortens the segments and improves the variance at the cost of a resolution decrease.
Clearly, there is a trade off between the number of averages and resolution. Here, as we deal with long data sequences, and to obtain more accurate averages is preferred over higher frequency resolution in the final spectra. In particular we deal with $N = o(10^{10})$ with a potential frequency resolution of $\Delta f = o(10^{-3})$ Hz: since the axion signal linewidth is of the order of 10 kHz, we can avevrage up to $o(10^7)$ peridograms and still have a resolution that allows us to spot an excess power at the frequency corresponding to the axion signal. The key point of the Bartlett method is then an improvement of the power resolution, meaning a reduction of the frequency noise.

4.3.2 Preliminary spectrum evaluation and time fluctuations

Thanks to the Bartlett method, we are able now to move from the time domain to the frequency domain for the time series of any run. In order to have an optimized data analysis, we decided to divide the time series into segments of $M = 16384$ samples each. This choice is in agreement with the dimension of the created time series files, as defined in Section 4.1.3, allowing us to average $K = 512$ peridograms for each saved file. This peridogram dimension has been chosen since it is small enough for the analysis, leading to a bin width BW of:

$$BW = \frac{1}{t_M} = \frac{f_{\mathrm{ADC}}}{M} \simeq 268.6\,\mathrm{Hz} \tag{4.16}$$

where t_M is the time required to acquire M time samples and f_{ADC} is the ADC sampling rate.
For each file, corresponding to 2 s-duration data acquisition, an averaged estimate is generated and saved for further analysis. Each Fourier Transform (FT) is therefore defined in the range $[-f_{\mathrm{ADC}}/2 : f_{\mathrm{ADC}}/2]$. The typical spectrum obtained averaging peridograms for a Thermal (blue) run and a Vacuum (red) run is presented in Figure 4.3. The shown spectra are centred at zero frequency, corresponding to the local oscillator frequency f_{LO}, while the cavity peak is centred approximately at 1 MHz. Then, at frequencies near to zero, some small peaks are visible in the spectrum: they are the result of IF processes and the power value in these bins is unreliable. Frequency region $[-200 : 200]$ kHz is neglected for further analysis. Note the filters' effect, that will be further discussed in Section 4.3.3, that suppress spectral components above ~ 1.7 MHz.

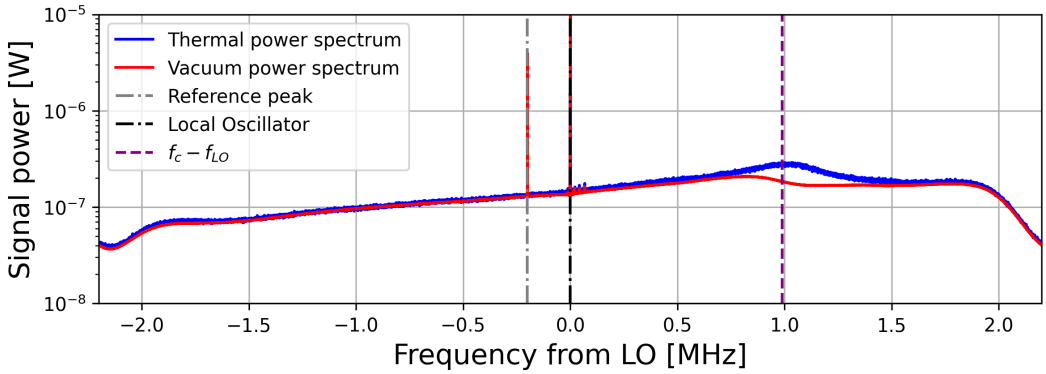

Figure 4.3: Example of the reconstructed spectrum for the thermal (blue) and vacuum (red) runs in the down-converted frequency range: we highlighted the reference peak, only visible in the vacuum runs, and the cavity frequency of resonance, demodulated at about 1 MHz

The spectrum displays also the peak corresponding to reference signal, exactly 200 kHz below f_{LO}. This signal is sent using SG1 from line L1, as shown in Figure 3.6b, to monitor the receiver gain. As detailed in Section 4.3.3 in case the TWPA exhibits instabilities during the acquisition, we are able to modify the spectra according to the measured gain variation. In Figure 4.4 we show the result of integration in 1 kHz window centred around the signal reference peak frequency for each block in run 668. The data can be smoothed by application of the Savitzky-Golay filter (SG), based on a third degree polynomial function and an integration window of about two minutes. The Savitsky-Golay is a digital filter able to perform a smoothing of the data by fitting successive subsets of adjacent data points with a low-degree polynomial using least squares[50]. Each averaged spectrum is then divided by the normalized value of the smoothed curve retrieved using the SG filter: this will create spectra that are not affected by the TWPA gain instabilities over time.

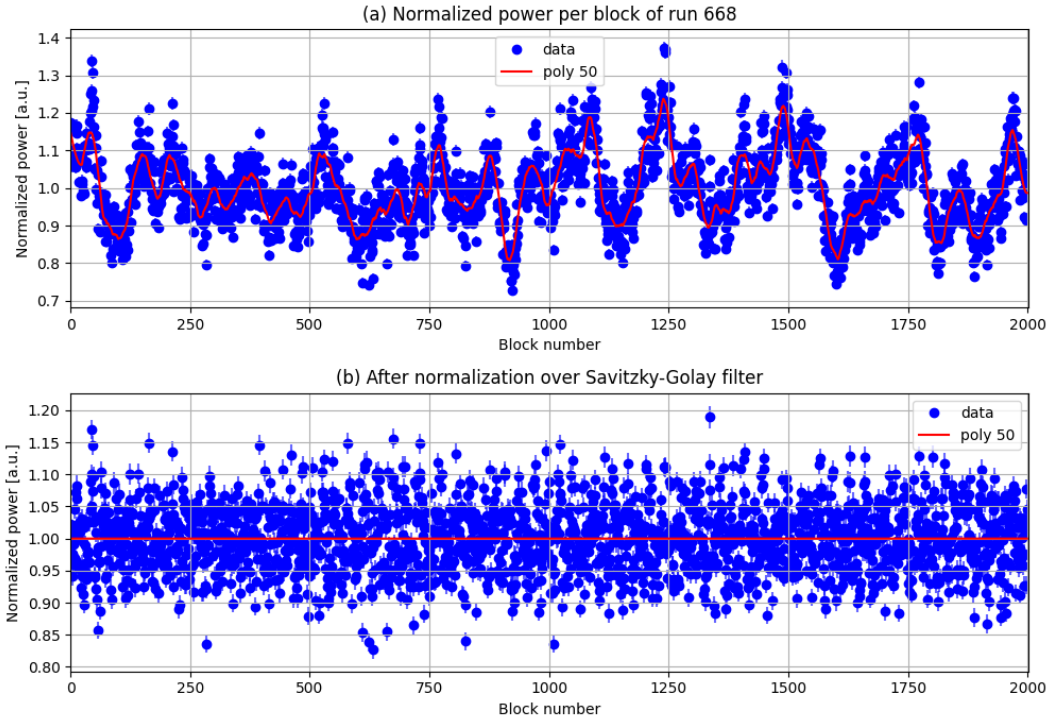

Figure 4.4: Time evolution of the reference peak power with the Savitsky-Golay filter smoothing (a) and the same after correction (b)

4.3.3 Accounting for spectral modulations

Additional effects that need to be taken into account to reconstruct the power spectrum at the cavity output are the TWPA gain dependence on frequency and the filter cuts. In practice, for each run, we estimate both the TWPA gain and the filter

attenuation. The spectrum is then divided by these values at each frequency value. Other additional effects, introduced by other receiver components, are responsible for other non-uniform signal amplitude w.r.t. frequency: they can be taken into consideration for a more accurate spectrum reconstruction at the cavity exit. These effects have been estimated to be under 1% of the power and are therefore neglected.

The TWPA amplifier gain, as previously detailed in Section 3.4.1, exhibits significant ripples. Even though the spectra cover a rather small frequency window of around ~ 5 MHz, when the TWPA gain is large, it can not be considered as constant in the frequency range near to the cavity. In order to evaluate its gain over the frequency, we select the TWPA resonance peak in the aforementioned frequency region and we fit it using the typical Fano resonance formula: we are not interested on the parameters of the fit, but only on the resonance profile.
Given the presence of a deep at the cavity frequency, we introduced a systematic procedure: we perform a preliminary fit on the gain profile, in order to have a first raw estimation of the resonance parameters. Then we select the region $[f_G - 3\sigma_G : f_c - 5\sigma_c] \cup [f_c + 5\sigma_c : f_G + 3\sigma_G]$, where f_c, f_G are respectively the cavity and the TWPA gain maximum frequency, and σ_c, σ_G their standard deviations: in this window we can perform the final fit, as shown in Figure 4.5(right). The introduction of this frequency window aims to suppress the zones of the gain that disturb the correct behaviour of a resonance, due to the TM_{030} and TM_{031} cavity modes absorption. In Figure 4.5(left) one can clearly see the absorption due to the aforementioned modes, represented by the two deeps.

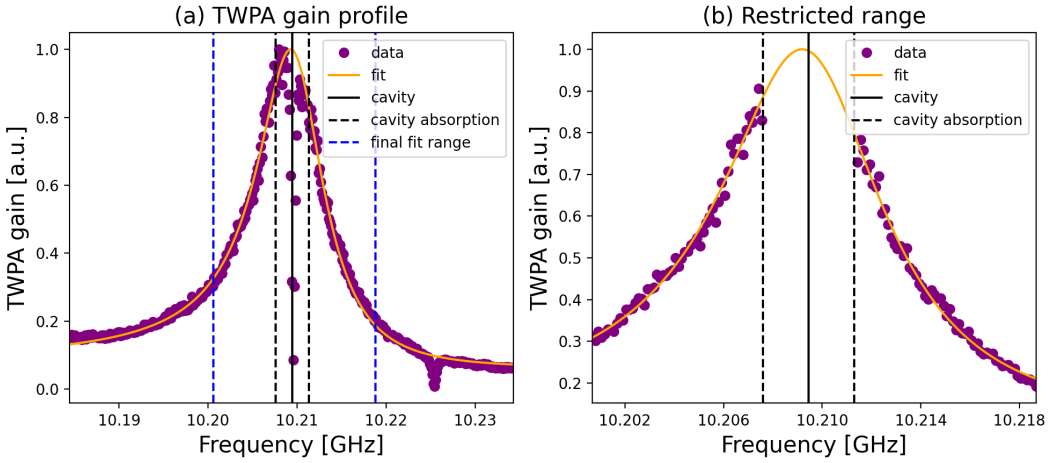

Figure 4.5: TWPA gain profile. (a) Full data plot, including data corresponding to the TM_{030} mode frequency, visible at the max of TWPA gain and of the TM_{031} mode, around 1.5 MHz higher. (b) Plot without the data points around TM_{030} and TM_{031} mode frequency, and related Fano figure fit curve.

As concerns the low pass filters, cutting at 1.7 MHz, we cannot rely on the gain profile

supplied by the manufacturer. The measured transfer function we used for spectra reconstruction is shown in Figure 4.6. This component's effect is to progressively suppress frequencies above 1.8 MHz, slightly higher than the manufacturer's predictions, while lower frequencies signals are attenuated by less than 10%. The 8-poles nature of the filter should in principle ensure a constant gain decrease for frequencies above 1.8 MHz, but Figure 4.6 shows the presence of a slight deflection from the constant decrease at about 2.2 MHz. This effect can be explained by an electronic phenomenon called aliasing, for which two different frequency components, one the multiple of the other, become indistinguishable if sampled at a too low frequency.

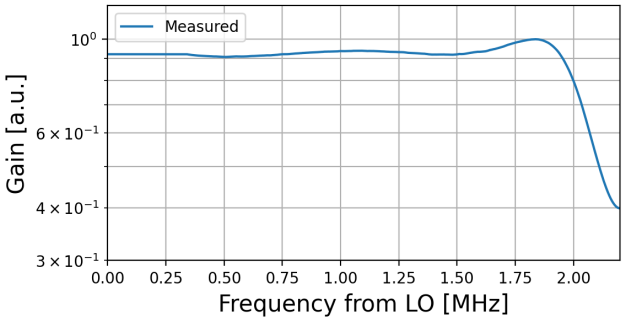

Figure 4.6: Behaviour of the 1.7 MHz low-pass filter in the down-converted range

4.4 Data quality cuts

Once the spectra have been corrected, a further step is to check the integrity of the data. The runs in which we are not able to reliably evaluate the power spectrum, as for instance those in which the cavity frequency was not stable during the acquisition, are flagged. In the data acquisition process, we used to check the cavity frequency before and after the vacuum run, to check if whether the cavity frequency varied. We can however monitor the cavity frequency during the overall acquisition to learn more about the sources of the change. This is accomplished using the vacuum spectra relative to a time series' sequence of approximatively 38 s, i.e. averaging together 20 files' spectra.
For a better cavity frequency estimation, we can use the spectral power expected behaviour as a fitting formula for each 38 s spectrum, as introduced in previous Sections. In order to take into account also a slight frequency dependence of the ADC, a linear trend is added to the Lorentzian profile, resulting in the formula:

$$F(\nu) = g^2 \frac{|\nu - a + ib|^2}{|\nu - c + id|^2} + f(\nu - c) \tag{4.17}$$

where a, b, c, d, f, g are fitting parameters. In this model the cavity frequency coincides with the parameter c: representative results of this parameter's behaviour

among the run are reported in Figure 4.7. A few runs are characterized by a random distribution of c (see for instance panel a, run 696), in five runs jumps are observed at some point (panel b, run 700), and for four of them an almost continuous drift is shown (panel c and d, runs 648 and 702 respectively).

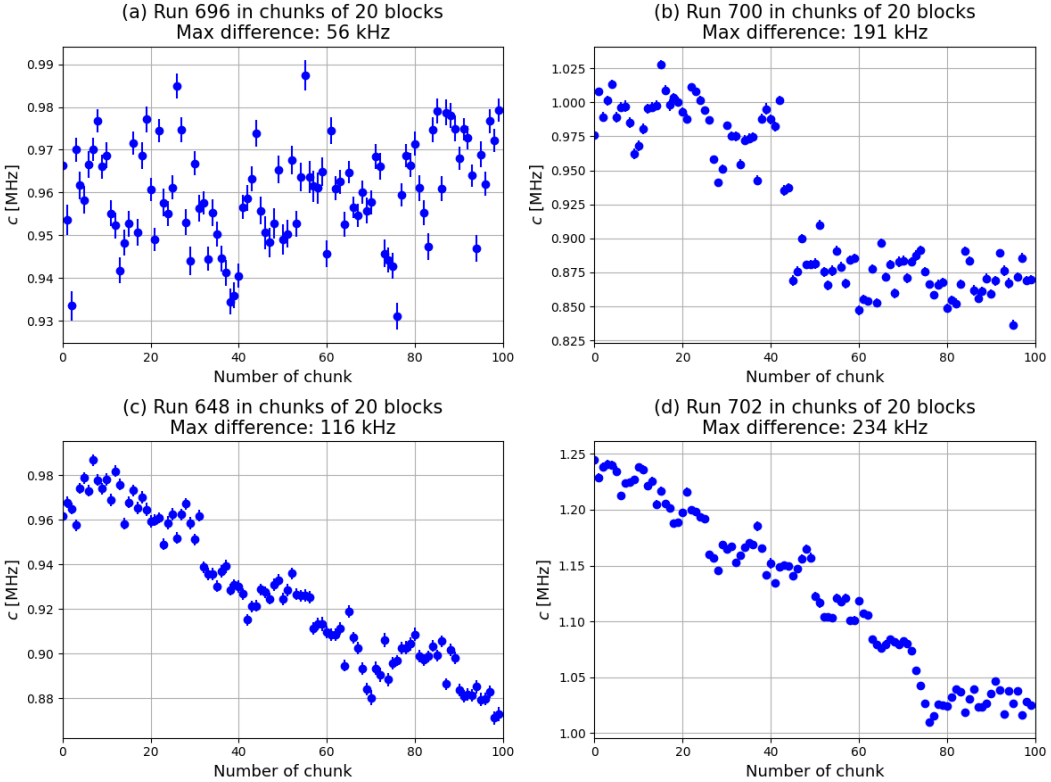

Figure 4.7: Behaviour of the cavity frequency of resonance, demodulated at 1MHz, obtained by fitting the vacuum spectra with equation 4.17. They have been classified as: (a) random in a reasonable range, (b) experiencing a jump, (c) showing a shift and (d) experiencing both a shift and a jump

Thanks to this analysis we were able to spot three runs with significant frequency instabilities, in addition to those flagged during the data acquisition. Given the different cavity frequency, we decided to operate as follows: runs experiencing a jump are divided into chunks corresponding to the different cavity positions, while in the other cases spectra remain unchanged, due to lack of information of what really happened during the acquisition.

The second cut is to be performed on the spectrum bins. One common issue is the contamination of the intermediate frequency (IF) arising from narrowband interference in the mixer, which leads to a systematic presence or absence of signal in these fixed bins. This effect can distort the statistical properties of the spectra, which are

the target of our analysis. In order to mitigate these effects, a systematic procedure is employed to identify and remove these contaminated IF bins from the data.[17]
The first step is to take the average of each 1000 blocks, in order to obtain all groups of the same size: averaging enhances the visibility of any sharp features due to narrowband interference. Then each spectrum is truncated in the interval $[0.3 : 1.7]$ MHz, which includes a sufficient number of bins on either side of the cavity frequency. This allows for application of the SG filter with reliable values also on the boundaries. Now we want to identify very sharp peaks corresponding to the IF frequency, and therefore we need to use a low-pass filter. For this reason we apply a Savitzky-Golay (SG) filter with a polynomial degree of 6 and a 50 kHz window on the averaged spectra. As previously described, the SG filter smooths the data by preserving large-scale spectral features, therefore we can identify interference contaminated bins by looking at the statistics. We then divide the averaged spectrum by the SG filter output and subtract one: the result is a transformed spectrum, whose statistics is Gaussian with a mean of zero and a standard deviation σ_{IF}, defined as:

$$\sigma_{\mathrm{IF}} = (N_{\mathrm{IF}} \Delta\nu_b \tau)^{-1/2} \tag{4.18}$$

where N_{IF} is the number of spectra in the group, $\Delta\nu_b$ is the bin width and τ is the observation time per bin. We can then look at bins that exceed a predefined threshold, set at $4.5\,\sigma_{IF}$, which are then flagged as potentially contaminated by interference. Given the large number of bins involved, which in the restricted range is 5212, it is statistically unlikely that more than a tiny fraction exceeds this threshold due to random fluctuations, and they are therefore considered significant.
Finally, we consider that interference may affect not only individual bins but also adjacent bins, due to the possible leakage at similar frequencies: bins adjacent to those flagged by the threshold are also marked as contaminated. This is a purely conservative approach, but for the axion search, a single bin is irrelevant, and a more reliable power estimate is preferred.
This process is iterative: at each step we identify contaminated bins and calculate the spectral baseline. Typically, only two or three iterations are needed to converge, resulting in a robust identification of all contaminated bins. After processing each group of spectra, the results are compared and the final list of contaminated bins is retrieved using the majority rule on the lists of single groups and contains 36 bins. Given the unreliability of these flagged bins in their power estimation, they are excluded in all the power spectra.

4.5 Axion discrimination

Once the spectra have been corrected and the problematic bins have been removed, the data are ready for the search of possible axion signals. In haloscope search, we expect the axion signal to appear as a small narrowband power excess at some frequency. From a statistical point of view, we test the null hypothesis H_0, which assumes the absence of an axion signal.

In order to spot a signal, the main idea is to look for excess power on some bins corresponding to the axion linewidth, previously evaluated in Section 2.1.3. From a practical point of view, we evaluate the spectrum baseline and look at the residuals behaviour. In presence of an axion signal, we expect to have a detectable statistical anomaly and therefore we will be able to reject the null hypothesis H_0 of pure noise.

Two main approaches are used in literature to evaluate the spectral baseline: using the predicted behaviour of the spectra, or using a general low-pass filter, and in our case the Savitzky-Golay (SG) filter, with a sufficiently large window.

The first approach is more reliable, since it allows to completely describe the physical system and to perform a more robust statistical analysis. The expected behaviour of the spectrum near to the cavity can be physically described by equation 4.17 in the absence of axion conversion: this formula can be used to fit the spectrum and therefore provide the expected behaviour of the power baseline. Furthermore a χ^2 test can be performed on this expected distribution, with the null hypothesis being the absence of axion signal. This approach is expected to work within a small frequency window, as previously devised in previous QUAX$_{a\gamma}$ runs [51], but fails if applied to experiments in which the condition $Q_a \gg Q_L$ applies. Wider frequency windows require more sophisticated equations to correctly predict the ADC frequency attenuations and fitting function 4.17 fails. In our experiment the cavity quality factor is much lower than the axion one, and a frequency window of at least 500 kHz is required in order to contain the relevant frequencies amplified by the cavity: this window is too large to take into account the variations in power baseline, therefore we are obliged to use the second approach and evaluate the spectral baseline using the SG filter.

The second approach requires the SG filter to use a sufficiently large integration window: since we want to detect axion excess power, an eventual presence of an axion signal must be ignored by the filter, while the cavity shape still has to be appreciated. A frequency window of approximatively 50 kHz has been chosen for the filter usage. The analysis, after the baseline evaluation using SG filter, is similar to the one used for the identification of out-of-statistics bins in Section 4.4: once each spectrum has been divided by the average, we can divide it by the baseline and subtract one. In Figure 4.9 the steps needed to obtain the normalized power excess spectrum are shown.

The result of this operation is the creation of a spectrum whose statistics is Gaussian in the absence of axion conversion, with mean zero and standard deviation $\sigma_p = 1/\sqrt{\Delta\nu_b\tau}$, with $\Delta\nu_b$ bin width and τ total integration time. So, in order to check if there is an axion signal in a normalized spectrum, we perform a χ^2 test on the Gaussian distribution of the residuals. In this case, one should observe out-of-statistics points in the histogram, which would concur to a significant increment of the χ^2 value for the same amount of degrees of freedom (d.o.f.). In order to have

a more reliable fit, we divide the residuals by the expected standard deviation, and therefore we expect the residuals behaviour to have mean zero and standard deviation equal to one. For each run a histogram is created and the χ^2 of the fitting Gaussian distribution is evaluated. A typical output is presented in Figure 4.8, where the obtained Gaussian fitting parameters μ_g and σ_g are compatible with the expected values.

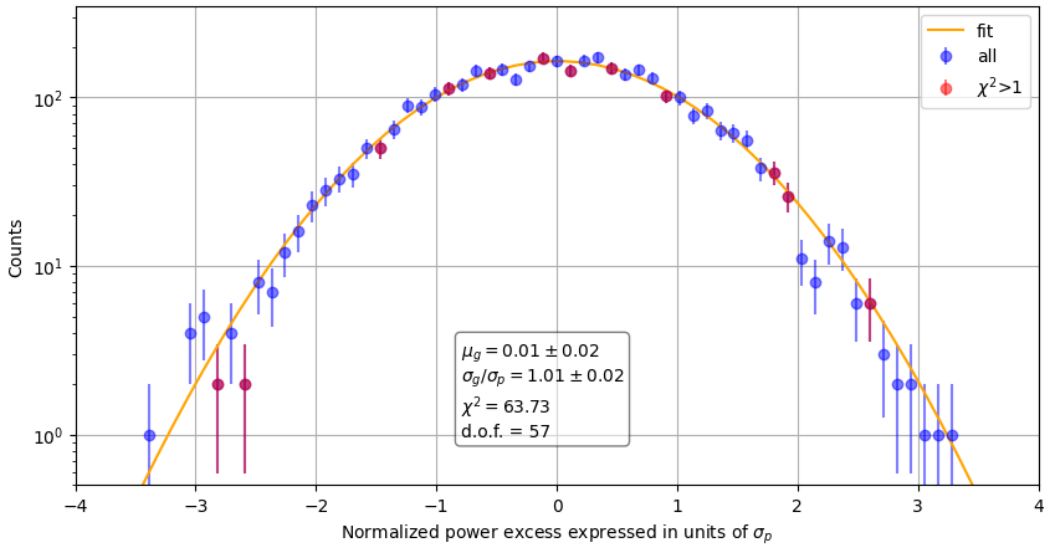

Figure 4.8: Histogram of power excess normalized to its expected standard deviation σ_p with the relative fit and the highlighted bins contributing to the χ^2

This analysis has been performed on all the averaged spectra, meaning for every run and for every block in the run, if the run has been divided as described in Section 4.4. With a selected significance threshold of $P_\alpha = 0.01$, we find that the null hypothesis H_0 is not rejected for each run, as indicated by the reported values in Table 4.1.[(3)]

4.6 Combining spectra: the grand spectrum

Up to now, we've been dealing with individual spectra referring to a fixed cavity frequency, here we want to combine them to produce an overall spectrum in the entire frequency range probed in a process known **vertical combination**. Bins belonging to different spectra but corresponding to the same frequency range will be combined to obtain the best SNR. In particular, as the range of each individual raw spectrum is three times the cavity linewidth, for a given frequency we can combine bins coming from at least three different spectra.

[(3)] In more sophisticated analysis, one should take into account the e effects of the SG filter on the spectra statistics: for the purpose of this thesis, we considered it to introduce no impacting effect

Run	χ^2	d.o.f	p-val	Run	χ^2	d.o.f	p-val	Run	χ^2	d.o.f	p-val
602	40	45	0.67	638	43	42	0.42	676	67	55	0.12
605	58	57	0.44	640	59	47	0.11	678	56	57	0.53
606	62	57	0.31	642	20	45	1.0	680	69	57	0.14
607	64	57	0.04	644	28	46	0.99	682	40	57	0.95
609	56	56	0.46	644	32	46	0.94	684	59	57	0.41
611	28	57	1.0	644	44	46	0.56	686	69	57	0.14
612	49	57	0.75	646	47	46	0.42	688	52	53	0.5
614	56	57	0.51	646	52	46	0.26	690	53	55	0.54
616	53	57	0.62	646	36	46	0.87	692	50	57	0.72
617	44	57	0.89	648	62	46	0.06	694	57	57	0.46
619	51	57	0.7	650	64	45	0.04	696	38	56	0.96
621	52	57	0.65	652	51	45	0.24	698	59	57	0.39
622	56	57	0.53	654	43	46	0.61	700	73	56	0.07
624	56	57	0.51	656	30	49	0.99	700	59	56	0.35
626	62	57	0.3	658	64	57	0.24	702	57	56	0.44
628	66	57	0.19	660	55	57	0.57	702	55	56	0.5
630	23	45	1.0	662	54	57	0.59	704	48	55	0.74
632	40	49	0.82	664	63	57	0.26	706	63	57	0.27
634	39	49	0.85	666	46	57	0.86	708	69	57	0.13
636	52	46	0.25	668	61	57	0.34	710	73	55	0.05
636	35	46	0.87	670	37	57	0.98	712	48	51	0.58
636	37	46	0.81	672	46	56	0.84	712	64	51	0.1
636	28	46	0.98	674	59	57	0.4	714	62	57	0.32

Table 4.1: Values of the χ^2 test performed on the power excess histograms, compared to the number of degreed of freedom (d.o.f.) and the relative p-value calculated.

The first step of this procedure requires to go back from the IF to the Radio Frequency (RF), then we can check how many spectra are overlapping on the same RF. This change of variable is necessary to correctly align the spectra. We can then group bins corresponding to the same frequency and we can take a weighted average of them. As these bins belong to spectra acquired under different conditions, primarily noise temperature and cavity parameters, we first have to rescale each spectrum, obtaining the so-called *rescaled spectrum* δ_i^s, where the j-th bin of the i-th spectrum is evaluated as:

$$\delta_{ij}^s = \frac{h\nu_{ci} N_i \Delta\nu_b \delta_{ij}^p}{P_{ij}}) \tag{4.19}$$

where δ_{ij}^p is the j-th bin of the i-th initial spectrum, ν_{ci} is the cavity frequency of the i-th run, $\Delta\nu_b$ is the bin size, N_i is the system noise defined as:

$$N_i = \frac{k_B T_i}{h\nu_{ci}} \tag{4.20}$$

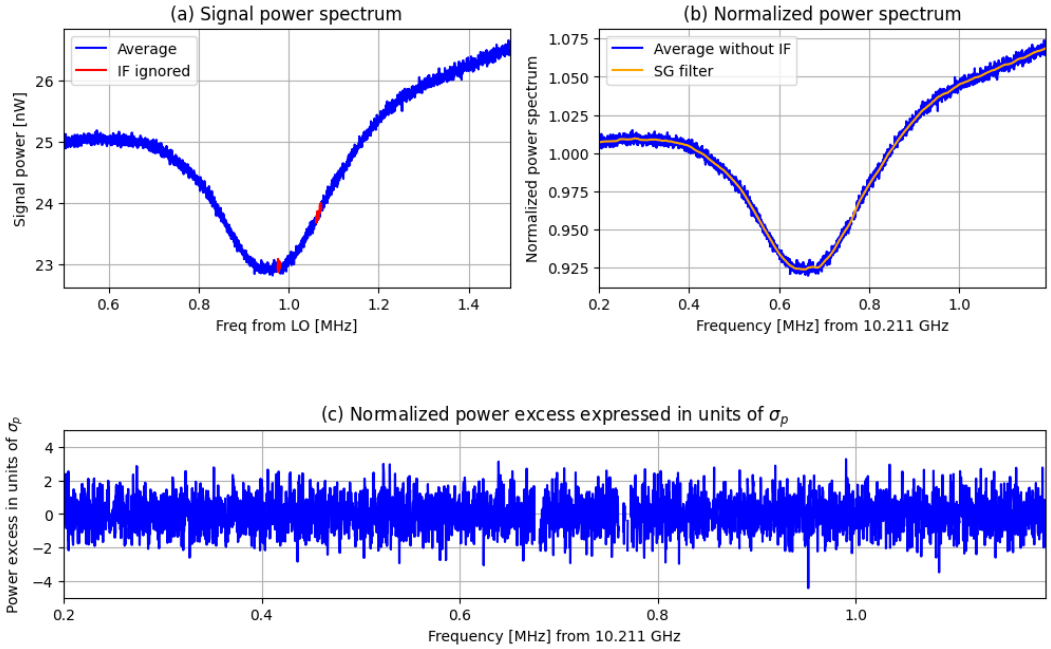

Figure 4.9: Steps required for the subtraction of the baseline using the SG filter: (a) spectrum of a single run with the flagged bins coming from the IF rejection procedure, (b) normalized spectrum with the SG output superimposed and (c) residuals behaviour of the normalized power spectrum divided by σ_p

where k_B is the Boltzmann constant and T_i is the noise temperature.[4] Finally P_{ij} is the total conversion power that we would obtain from a KSVZ axion signal confined to the j-th bin of the i-th spectrum:

$$P_{ij} = U_0 \left(\nu_{ci} \frac{\beta_i}{1+\beta_i} C_i \frac{Q_{Li}}{1 + \left(\frac{2(\nu_{ij} - \nu_{ci})}{\nu_{ci}} \right)^2} \right) \tag{4.21}$$

where C_i is the C-factor, Q_{Li}, β_i are cavity-dependent and U_0 is a constant energy factor defined as follows:

$$U_0 = g_\gamma^2 \frac{\alpha^2}{\pi^2} \frac{\hbar^3 c^3 \rho_a}{\Lambda_{\mathrm{QCD}}^4 \mu_0} B_0^2 V \tag{4.22}$$

where g_γ is the KSVZ coupling factor and α is the fine structure constant. Residuals of the spectrum are rescaled accordingly as:

$$\sigma_{ij}^s = \frac{h \nu_{ci} N_i \Delta\nu_b \sigma_{ij}^p}{P_{ij}} \tag{4.23}$$

[4] This system noise can be further corrected by introducing a dependence on the bin of each spectrum, based on the varying noise temperature, but here we take this variation to be small.

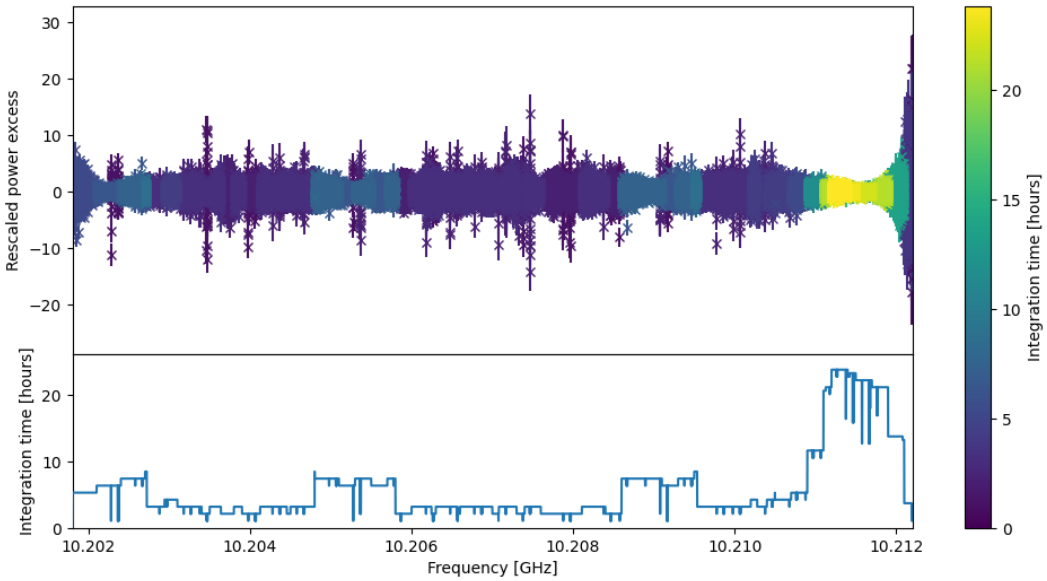

Figure 4.10: Behaviour of the combined spectrum δ^c with a colour palette in order to highlight the integration time per a specific bin

With the rescaled spectrum we can reliably assess the sensitivity of each bin. As they can be considered as independent Gaussian random variables, we can average them using a Maximum Likelihood (ML) approach, which provides a statistically optimal way to combine data from different sources with varying degrees of reliability. Thanks to this averaging, we are able to create the so-called *combined spectrum* δ^c, which is mathematically retrieved using a weighted average whose weights are evaluated as:

$$w_{ij} = \frac{\left(\sigma^s_{ij}\right)^{-2}}{\sum_{i'}\sum_{j'}\left(\sigma^s_{i'j'}\right)^{-2}} \tag{4.24}$$

where the denominator ensures normalization. Then the ML estimate of the mean and standard deviation for each combined spectrum bin j can be retrieved using the usual weighted average:

$$\delta^c_j = \sum_{i'} w_{i'j}\delta^s_{i'j} \tag{4.25}$$

$$\left(\sigma^c_j\right)^2 = \sum_{i'} w^2_{i'j}\left(\sigma^c_{i'j}\right)^2 \tag{4.26}$$

A visual representation of the obtained combined spectrum is presented in Figure 4.10. As a further proof, we show the Gaussian distribution of the signal to noise ratio, defined as: $SNR = \delta^c_j/\sigma^c_j$ in Figure 4.11

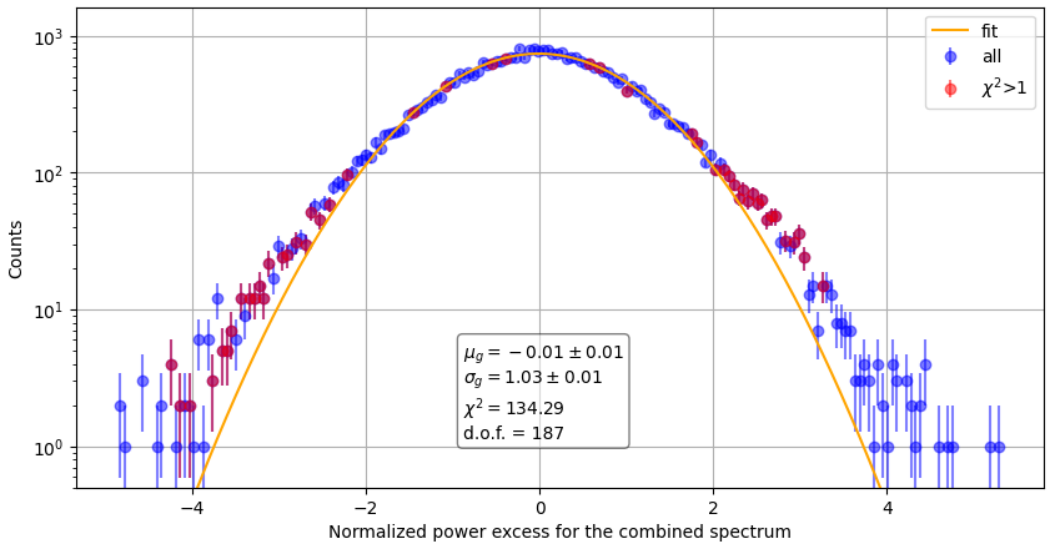

Figure 4.11: Gaussian distribution of the signal to noise ratios, showing that the estimated parameter are in accordance with those expected from a random variable

It is then common in haloscope data analysis to rebin the combined spectrum in order to have bins that could in principle contain most of the axion deposited power, usually using the expected signal linewidth $\Delta\nu_a$ as bin dimension. At $\sim$ 10 GHz frequency, $\Delta\nu_a \sim 10$ kHz $\gg BW$, thus we can merge adjacent bins to further improve the sensitivity. This procedure is also known as **horizontal combination** and brings to the so-called *grand spectrum*.

The grand spectrum is the ultimate spectrum, since it allows to reach the best possible SNR, given the acquired data. In particular we are interested in the grand spectrum signal to noise ratio SNR^g: a threshold on SNR^g is set and bins exceeding this threshold are flagged as potential axion signals. The grand spectrum SNR can be retrieved as:

$$\mathrm{SNR}_l^g = \frac{\sum_{q=q_i(l)}^{q_f(l)} \delta_q^c \left(\sigma_q^c\right)^{-2}}{\sqrt{\sum_{q=q_i(l)}^{q_f(l)} \left(\sigma_q^c\right)^{-2}}} \tag{4.27}$$

where $q_i(l) = l \cdot F$ and $q_f(l) = (l+1)F$ are respectively the initial and final integration points for a single grand spectrum bin l and F is the number of bins that we are integrating.
It is important to note that the axion search analysis conducted in this thesis work is simplified as the axion frequency distribution has not been considered.

In our evaluation, as the axion signal is expected to have a linewidth of 10 kHz at 10 GHz, we integrate across $F = \lfloor \Delta_a / BW \rfloor = 37$ bins with a bin width $BW \simeq 268$ Hz. In Figure 4.12 we plot the grand spectrum SNR, in which an axion candidate

was found at 10.201934 ± 0.000005 GHz for a SNR threshold fixed to $\Theta = 3.455$. With the threshold set to this value, as suggested by [17], a signal candidate with $\mathrm{SNR}_C = 5.1$ is flagged with a 95% CL: this represent a compromise between the number of rescan candidates and the probability of detecting the axion, if present, as one can see in Figure 4.13.

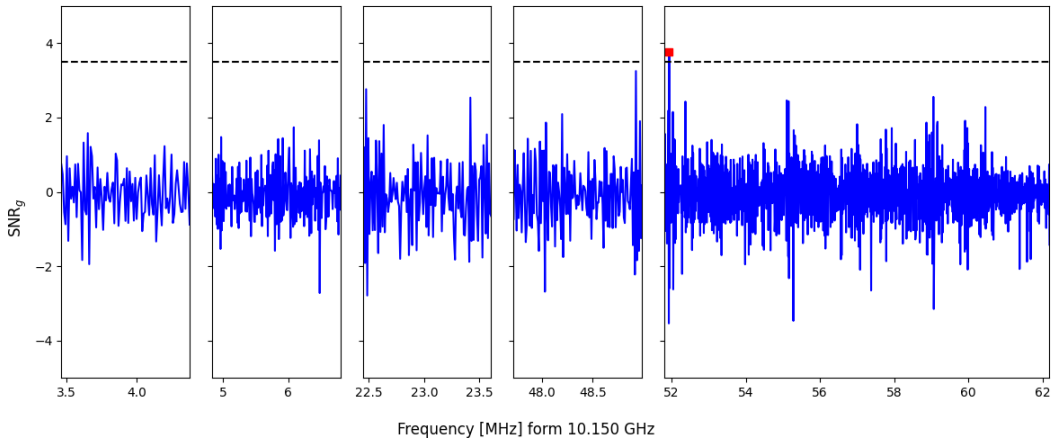

Figure 4.12: Grand spectrum SNR with the axion frequency candidate highlighted

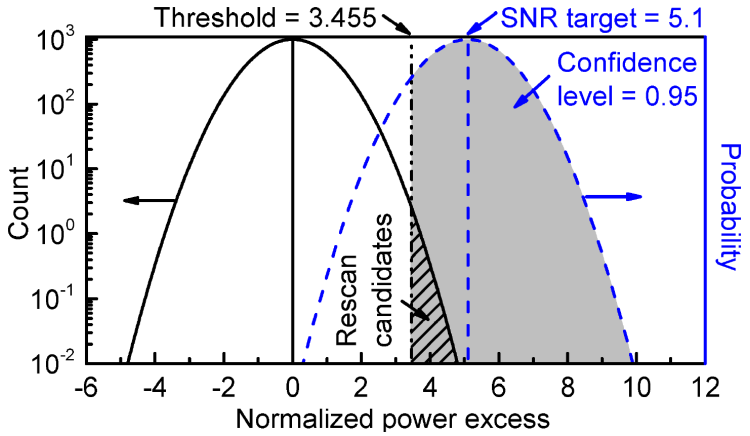

Figure 4.13: Schematic illustration of the relationship between the SNR target $\mathrm{SNR}_C = 5.1$ and the rescan threshold $\Theta = 3.455$. The solid black curve represents the expected standard normal distribution of the grand spectrum bins. The dashed blue curve, a Gaussian distribution with unit standard deviation and mean equal to SNR_C, represents the expected distribution of excess power in a single grand spectrum bin containing an axion signal. The threshold Θ, corresponding to the dot-dashed vertical line, defines the grey shaded region which represents the rescan candidates.

A sanity check for the grand spectrum is reported in Figure 4.14, where the grand spectrum residuals' histogram is well fitted by a Gaussian curve, whose mean is compatible with zero. There are however some limitations in the present analysis as we see that the obtained standard deviation σ_g is smaller than 1. This might be ascribed to the following reasons:

- we did not consider correlations between adjacent bins;
- the attenuation of the SG filter has not been considered;
- we neglected the axion frequency distribution in the grand spectrum evaluation

These aspects need to be taken into account to improve on the present analysis.

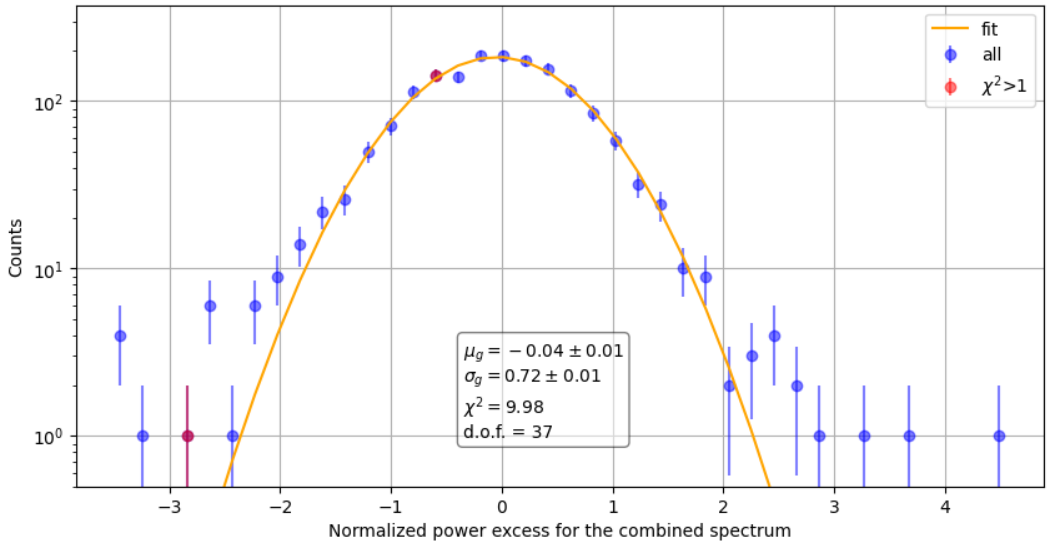

Figure 4.14: Gaussian behaviour of the grand spectrum signal to noise ratio SNR_g, having mean compatible with zero and standard deviation lower than one, as expected for the reasons described in the text [17]

4.7 Upper limit

During this thesis, it was not possible to rescan the frequency interval in which an axion candidate was found. In the full probed range from 10.202 GHz to 10.212 GHz, with exclusion of this small interval, we were able to set new limits on the axion-photon coupling coefficient $g_{a\gamma\gamma}$. This limit has been set for other four smaller frequency ranges, the same we show in Figure 4.12 for the grand spectrum.

The axion signal power for KSVZ axions P_{KSVZ} in the QUAX experiment is:

$$P_{\mathrm{KSVZ}} = \frac{g_\gamma^2 \nu_c B_0^2 C_{030} V}{\rho_{\mathrm{DM}}} \frac{\beta}{1+\beta} \frac{Q_L Q_a}{Q_L + Q_a} \approx 8.7 \times 10^{-24}\,\mathrm{W} \tag{4.28}$$

where the used parameters are: $C_{030} = 0.4$, $\langle B_0^2 \rangle = 50.2$ T, $V = 1.05$ cm^3, $\beta \sim 1.7$, $Q_L \sim 28000$ and $\nu_c \sim 10$ GHz.

A rough estimation of the SNR that we have for this KSVZ axion needs the average noise estimation. Since the noise power in the detector is given by the Dicke radiometer equation, we estimate the residual standard deviation, $\sigma'_{\rm res}$, of the noise power for an optimal bin width matching the axion linewidth as:

$$\sigma'_{\rm res} \approx \sigma_{\rm Dicke}\Big|_{\Delta\nu=\Delta\nu_a} = k_B T_s \sqrt{\frac{\Delta\nu}{\Delta t}} \approx 1.5 \times 10^{-23}\,{\rm W} \tag{4.29}$$

evaluated for an integration time of 19000 seconds.

Given these quantities, the SNR for KSVZ axions is calculated approximatively:

$${\rm SNR}_{\rm KSVZ} = \frac{P_{\rm KSVZ}}{\sigma'_{\rm res}} \simeq 0.5 \tag{4.30}$$

This SNR value indicates that the detector's sensitivity is insufficient for a direct detection of the KSVZ axion, as the expected SNR is below unity.

To evaluate the upper limit, we follow an analysis which is very similar to the grand spectrum one: we aggregate power excesses from overlapping frequency bins across different runs and then we evaluate the most likely value of $g^2_{a\gamma\gamma}$ (denoted as $g^2_{a\gamma\gamma,{\rm calc.}}$) for each frequency, assuming that the true mean value is consistent across all runs:

$$g^2_{a\gamma\gamma,{\rm calc.}} = \frac{\sum_{ij} \frac{\delta^s_{ij} T_{ij}}{\sigma^2_{{\rm res},i}}}{\sum_{ij} \frac{T^2_{ij}}{\sigma^2_{{\rm res},i}}} \tag{4.31}$$

where: δ^s_{ij} is the known j-th bin of the i-th run residual, $\sigma_{{\rm res},i}$ is the standard deviation of the i-th run residuals, and finally T_{ij} is the axion expected power in the j-th bin of the j-th run. The corresponding standard deviation is:

$$\sigma^2(g^2_{a\gamma\gamma,{\rm calc.}}) = \frac{1}{\sum_{ij} \frac{T^2_{ij}}{\sigma^2_{{\rm res},i}}} \tag{4.32}$$

To establish the 90% C.L. upper limit on $g_{a\gamma\gamma}$, we compute it as:

$$g_{a\gamma\gamma,{\rm CL}} = \begin{cases} \sqrt{0.28\,\sigma(g^2_{a\gamma\gamma,{\rm calc.}})} & \text{if } g^2_{a\gamma\gamma,{\rm calc.}} < -\sigma(g^2_{a\gamma\gamma,{\rm calc.}}) \\ \sqrt{g^2_{a\gamma\gamma,{\rm calc.}} + 1.28\,\sigma(g^2_{a\gamma\gamma,{\rm calc.}})} & \text{if } g^2_{a\gamma\gamma,{\rm calc.}} > -\sigma(g^2_{a\gamma\gamma,{\rm calc.}}) \end{cases}$$

This condition ensures the physical constraint that $g^2_{a\gamma\gamma}$ cannot be negative, and the computation incorporates the statistical uncertainty of the measurement. The results of such calculation in the probed frequency ranges is presented in Figure 4.15 in which the KSVZ coupling constant is also reported.

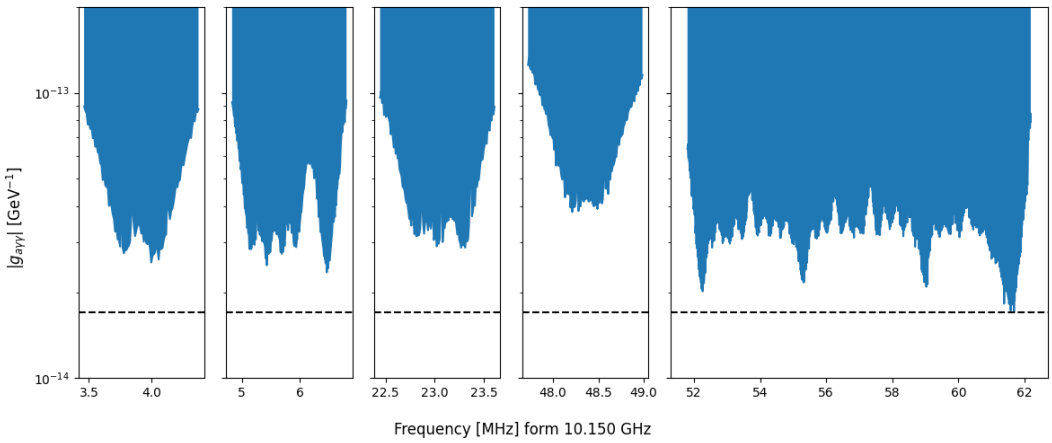

Figure 4.15: 90% CL upper limit on the coupling constant in the scanned frequency ranges. The dashed black line indicates the KSVZ coupling constant expected value.

Chapter 5

Conclusions

This thesis has been conducted within the QUAX$_{a\gamma}$ (QUest for AXions) experimental program, which aims to probe the existence of galactic axions in the high frequency range ($\sim$ 10 GHz) using a tunable dielectric cavity and an ultrasensitive cryogenic receiver. In this experiment, axions can be detected by exploiting their interaction with photons in the presence of a strong magnetic field. Axions convert to photons via the inverse Primakoff effect inside a microwave resonator, which gives a resonant enhancement of the signal.

The microwave cavity used in the experiment is a copper cylinder hosting a sapphire shell, which enables high effective volumes at high frequencies while maintaining high quality factors. This is crucial for enhancing the detector sensitivity to potential axion signals. The cavity is comprised of two halves that are separated by means of a clamshell mechanism, which has been demonstrated to allow cavity frequency tuning across the range $10.153 - 10.212$ GHz.
A Traveling Wave Parametric Amplifier (TWPA) is used as the first step in the signal amplification chain. TWPAs are superconducting amplifiers designed to introduce minimal noise, barely exceeding the standard quantum limit. These components, only recently introduced in the context of haloscope searches, are important as they reduce the noise temperature of the system and in turn improve the overall haloscope sensitivity.

To run an haloscope experiment, it is preferred to develop a fully automatic routine for data acquisition. For the QUAX experiment, computer programs have been developed to evaluate the receiver noise temperature and to measure the cavity parameters, mainly frequency and quality factor, within the run routine. This a necessary step, as the cavity frequency is modified by the tuning mechanism to probe for different axion masses. In addition, the TWPA amplifier operational parameters need also to be adjusted at each cavity tuning step due to the frequency dependence of its gain and instabilities.
Another computer program has been devised for collection of raw cavity spectra when all the RF sources have been switched off. Both in-phase and quadrature signals

are acquired by the ADC, after the frequency down-conversion at the intermediate frequency (IF). These are the data of interest for the axion search, which are analysed to set limits in the axion-photon exclusion plot in case a signal is not found.

In this thesis, data acquired during a two-week duration experimental run, in May-June 2024, have been analysed. The steps of the analysis procedure entail a preliminary analysis of the raw spectra to identify compromised spectra and specific bins affected by IF noise. These spectra are excluded from further analysis. Spectra are then prepared for the excess noise search, through normalization to the average baseline and successive removal of the spectral structure via the Savitzky-Golay filter, a commonly used smoothing algorithm. A set of dimensionless processed spectra described by a Gaussian distribution is therefore generated. Finally, through so-called vertical and horizontal combination procedures, the processed spectra are then aligned in frequency to construct a single, grand spectrum across the whole scan range.
Even though the analysis is missing some steps, including the assessment of the expected axion signal through the axion energy distribution, the grand spectrum has been used to set a preliminary limit on the axion-photon coupling constant.
No axion candidate signal has been found in the probed frequency range of $10.202 - 10.212$ GHz, corresponding to axion masses of $42.19 - 42.23\,\mu$eV, as long as other four smaller frequency regions, for a total covered range of ~ 15 MHz. The minimum found value sets a limit $g_{a\gamma\gamma,\mathrm{CL}} < 1.8 \cdot 10^{-14}$ GeV^{-1}, which is almost at the level of the benchmark KSVZ axion models.

Planned upgrades, which will regard both the hardware, as for instance a more reliable tuning mechanism and a more powerful magnet, and the software (control and acquisition computer programs) of the experiment, will allow for improving both the sensitivity and the search speed of 3 MHz/day that were accomplished in the experimental run presented in this thesis.

Bibliography

[1] J.-c. Hwang and H. Noh, "Axion as a cold dark matter candidate," *Physics Letters B*, vol. 680, no. 1, pp. 1–3, 2009.

[2] G. Carosi, G. Rybka, and K. Van Bibber, *Microwave cavities and detectors for axion research*. Springer, 2020.

[3] Y. K. Semertzidis and S. Youn, "Axion dark matter: How to see it?," *Science Advances*, vol. 8, no. 8, p. eabm9928, 2022.

[4] V. Baluni, "Cp-nonconserving effects in quantum chromodynamics," *Physical Review D*, vol. 19, no. 7, p. 2227, 1979.

[5] R. D. Peccei and H. R. Quinn, "Cp conservation in the presence of pseudoparticles," *Physical Review Letters*, vol. 38, no. 25, p. 1440, 1977.

[6] A. Sakharov, "Violation of cp invariance, c asymmetry, and baryon asymmetry of the universe," *Usp. Fiz. Nauk*, vol. 161, pp. 61–64, 1991.

[7] D. Samtleben, S. Staggs, and B. Winstein, "The cosmic microwave background for pedestrians: A review for particle and nuclear physicists," *Annu. Rev. Nucl. Part. Sci.*, vol. 57, no. 1, pp. 245–283, 2007.

[8] A. O. Sushkov, "Quantum science and the search for axion dark matter," *PRX Quantum*, vol. 4, no. 2, p. 020101, 2023.

[9] V. Cardoso, Ó. J. Dias, G. S. Hartnett, M. Middleton, P. Pani, and J. E. Santos, "Constraining the mass of dark photons and axion-like particles through black-hole superradiance," *Journal of Cosmology and Astroparticle Physics*, vol. 2018, no. 03, p. 043, 2018.

[10] M. Buschmann, C. Dessert, J. W. Foster, A. J. Long, and B. R. Safdi, "Upper limit on the qcd axion mass from isolated neutron star cooling," *Physical review letters*, vol. 128, no. 9, p. 091102, 2022.

[11] A. Friedland, M. Giannotti, and M. Wise, "Constraining the axion-photon coupling with massive stars," *Physical Review Letters*, vol. 110, no. 6, p. 061101, 2013.

[12] D. Fordham and I. Lopes, "Constraints on the axion-photon coupling using stellar modeling," *Physical Review D*, vol. 109, no. 12, p. 123007, 2024.

[13] L. Di Luzio, M. Giannotti, E. Nardi, and L. Visinelli, "The landscape of qcd axion models," *Physics Reports*, vol. 870, 2020.

[14] P. Sikivie, "Experimental tests of the" invisible" axion," *Physical Review Letters*, vol. 51, no. 16, p. 1415, 1983.

[15] C. Hagmann, P. Sikivie, N. Sullivan, and D. Tanner, "Results from a search for cosmic axions," *Physical Review D*, vol. 42, no. 4, p. 1297, 1990.

[16] C. Hagmann, D. Kinion, W. Stoeffl, K. Van Bibber, E. Daw, H. Peng, L. J. Rosenberg, J. LaVeigne, P. Sikivie, N. Sullivan, *et al.*, "Results from a high-sensitivity search for cosmic axions," *Physical Review Letters*, vol. 80, no. 10, p. 2043, 1998.

[17] B. M. Brubaker, *First results from the HAYSTAC axion search*. PhD thesis, Yale University, 2017.

[18] Y. K. Semertzidis, J. E. Kim, S. Youn, J. Choi, W. Chung, S. Haciomeroglu, D. Kim, J. Kim, B. Ko, O. Kwon, *et al.*, "Axion dark matter research with ibs/capp," *arXiv preprint arXiv:1910.11591*, 2019.

[19] C. Braggio, G. Cappelli, G. Carugno, N. Crescini, R. Di Vora, M. Esposito, A. Ortolan, L. Planat, A. Ranadive, N. Roch, *et al.*, "A haloscope amplification chain based on a traveling wave parametric amplifier," *Review of Scientific Instruments*, vol. 93, no. 9, 2022.

[20] C. O'Hare, "cajohare/axionlimits: Axionlimits." `https://cajohare.github.io/AxionLimits/`, July 2020.

[21] K. Zioutas, S. Andriamonje, V. Arsov, S. Aune, D. Autiero, F. Avignone, K. Barth, A. Belov, B. Beltrán, H. Bräuninger, *et al.*, "First results from the cern axion solar telescope," *Physical review letters*, vol. 94, no. 12, p. 121301, 2005.

[22] R. Barbieri, C. Braggio, G. Carugno, C. S. Gallo, A. Lombardi, A. Ortolan, R. Pengo, G. Ruoso, and C. C. Speake, "Searching for galactic axions through magnetized media: The quax proposal," *Physics of the Dark Universe*, vol. 15, pp. 135–141, 2017.

[23] D. F. Jackson Kimball, S. Afach, D. Aybas, J. Blanchard, D. Budker, G. Centers, M. Engler, N. Figueroa, A. Garcon, P. Graham, *et al.*, "Overview of the cosmic axion spin precession experiment (casper)," in *Microwave Cavities and Detectors for Axion Research: Proceedings of the 3rd International Workshop*, pp. 105–121, Springer, 2020.

[24] G. Gabadadze and M. Shifman, "Qcd vacuum and axions: What's happening?," *International Journal of Modern Physics A*, vol. 17, no. 26, pp. 3689–3727, 2002.

[25] I. P. Stern, ADMX, and A.-H. collaborations, "Axion dark matter searches," in *AIP Conference Proceedings*, vol. 1604, pp. 456–461, American Institute of Physics, 2014.

[26] M. S. Turner, "Periodic signatures for the detection of cosmic axions," *Physical Review D*, vol. 42, no. 10, p. 3572, 1990.

[27] B. Beltran, "Search for solar axions: The cast experiment at cern," *arXiv preprint hep-ex/0507007*, 2005.

[28] H. Padamsee, "Superconducting radiofrequency technology for accelerators: state of the art and emerging trends," 2023.

[29] D.-H. Han, Y.-S. Kim, and M. Kwon, "Two port cavity q measurement using scattering parameters," *Review of scientific instruments*, vol. 67, no. 6, pp. 2179–2181, 1996.

[30] H. K. Hughes, "The physical meaning of parseval's theorem," *American Journal of Physics*, vol. 33, no. 2, pp. 99–101, 1965.

[31] D. M. Pozar, *Microwave engineering: theory and techniques*. John wiley & sons, 2021.

[32] Y. Lee, B. Yang, H. Yoon, M. Ahn, H. Park, B. Min, D. Kim, and J. Yoo, "Searching for invisible axion dark matter with an 18 t magnet haloscope," *Physical review letters*, vol. 128, no. 24, p. 241805, 2022.

[33] R. Di Vora *et al.*, "High frequency dark matter axion search with very high-quality factor dielectric resonators in the quax-aγ experiment," 2022.

[34] A. Clark, J. Ekin, D. Vecchia, and L. Goodrich, "Standard reference materials: Critical current measurements on an nbti superconducting wire standard reference material," 1984.

[35] M. Jewell, A. Leder, K. Backes, X. Bai, K. van Bibber, B. Brubaker, S. Cahn, A. Droster, M. H. Esmat, S. Ghosh, *et al.*, "New results from haystac's phase ii operation with a squeezed state receiver," *Physical Review D*, vol. 107, no. 7, p. 072007, 2023.

[36] S. Ahn, J. Kim, B. I. Ivanov, O. Kwon, H. Byun, A. F. van Loo, S. Park, J. Jeong, S. Lee, J. Kim, *et al.*, "Extensive search for axion dark matter over 1 ghz with capp's main axion experiment," *Physical Review X*, vol. 14, no. 3, p. 031023, 2024.

[37] K. Van Bibber, C. Hagmann, W. Stoeffl, E. Daw, L. Rosenberg, P. Sikivie, N. Sullivan, D. Tanner, D. Moltz, R. Tighe, *et al.*, "Status of the large-scale dark-matter axion search," *Sources of Dark Matter in the Universe*, p. 248, 1995.

[38] D. Alesini, C. Braggio, G. Carugno, N. Crescini, D. D'Agostino, D. Di Gioacchino, R. Di Vora, P. Falferi, U. Gambardella, C. Gatti, *et al.*, "Realization of a high quality factor resonator with hollow dielectric cylinders for axion searches," *Nuclear Instruments and Methods in Physics Research Section A: Accelerators, Spectrometers, Detectors and Associated Equipment*, vol. 985, p. 164641, 2021.

[39] C. Braggio, G. Carugno, R. Di Vora, A. Ortolan, G. Ruoso, and D. Seyler, "A tunable clamshell cavity for wavelike dark matter searches," *Review of Scientific Instruments*, vol. 94, no. 4, 2023.

[40] A. Rettaroli, D. Alesini, D. Babusci, C. Braggio, G. Carugno, D. D'Agostino, A. D'Elia, D. Di Gioacchino, R. Di Vora, P. Falferi, *et al.*, "Search for axion dark matter with the quax–lnf tunable haloscope," *Physical Review D*, vol. 110, no. 2, p. 022008, 2024.

[41] J. J. Bautista, "Hemt low-noise amplifiers," *Lownoise systems in the deep space net work/Ed. by Macgregor S. Reid.–Jet propulsion laboratory, California institute of technology*, 2008.

[42] P. Borghi, "Measuring the performance of a reversed kerr traveling-wave parametric amplifier for quantum sensing in axion dark matter search,"

[43] N. Crescini, D. Alesini, C. Braggio, G. Carugno, D. D'Agostino, D. Di Gioacchino, P. Falferi, U. Gambardella, C. Gatti, G. Iannone, *et al.*, "Axion search with a quantum-limited ferromagnetic haloscope," *Physical Review Letters*, vol. 124, no. 17, p. 171801, 2020.

[44] J. W. Yoon and R. Magnusson, "Fano resonance formula for lossy two-port systems," *Optics Express*, vol. 21, no. 15, pp. 17751–17759, 2013.

[45] D. Rieger, S. Günzler, M. Spiecker, A. Nambisan, W. Wernsdorfer, and I. Pop, "Fano interference in microwave resonator measurements," *Physical Review Applied*, vol. 20, no. 1, p. 014059, 2023.

[46] L. Zhong, S. Al Kenany, K. Backes, B. Brubaker, S. Cahn, G. Carosi, Y. Gurevich, W. Kindel, S. Lamoreaux, K. Lehnert, *et al.*, "Results from phase 1 of the haystac microwave cavity axion experiment," *Physical Review D*, vol. 97, no. 9, p. 092001, 2018.

[47] D. Alesini, D. Babusci, C. Braggio, G. Carugno, N. Crescini, D. D'Agostino, A. D'Elia, D. Di Gioacchino, R. Di Vora, P. Falferi, *et al.*, "Search for galactic axions with a high-q dielectric cavity," *Physical Review D*, vol. 106, no. 5, p. 052007, 2022.

[48] E. Por, M. van Kooten, and V. Sarkovic, "Nyquist–shannon sampling theorem," *Leiden University*, vol. 1, no. 1, pp. 1–2, 2019.

[49] D. Alesini, "Power coupling," *arXiv:1112.3201 [physics.acc-ph]*, 2011.

[50] R. W. Schafer, "What is a savitzky-golay filter?[lecture notes]," *IEEE Signal processing magazine*, vol. 28, no. 4, pp. 111–117, 2011.

[51] R. Di Vora, A. Lombardi, A. Ortolan, R. Pengo, G. Ruoso, C. Braggio, G. Carugno, L. Taffarello, G. Cappelli, N. Crescini, *et al.*, "Search for galactic axions with a traveling wave parametric amplifier," *Physical Review D*, vol. 108, no. 6, p. 062005, 2023.